

Supplementary information for

A thin crème brûlée rheological structure for the Eastern California Shear Zone

Shaozhuo Liu^{1*}, Zheng-Kang Shen², Roland Bürgmann³, and Sigurjón Jónsson¹

¹ King Abdullah University of Science and Technology, Thuwal, Makkah 23955, Saudi Arabia

² Department of Earth, Planetary, and Space Sciences, University of California, Los Angeles, California 90095-1567, USA

³ Department of Earth and Planetary Science, University of California, Berkeley, California 94720-4767, USA

*shaozhuo.liu@kaust.edu.sa

Table of Contents

A THIN CRÈME BRÛLÉE MODEL FOR THE EASTERN CALIFORNIA SHEAR ZONE	ERROR!
BOOKMARK NOT DEFINED.	
S1. SUPPLEMENTARY DATA	2
S1.1 A UNIFIED POSTSEISMIC GPS POSITION TIME SERIES DATASET FOR THE 1992 AND 1999 EVENTS	2
<i>s1.1.1 Subsampling NGL GPS time series</i>	3
<i>s1.1.2 Correcting residual postseismic transients</i>	3
<i>s1.1.3 Combining GPS time series</i>	4
<i>s1.1.4 New GPS time series</i>	5
S1.2 POSTSEISMIC GPS POSITION TIME SERIES DATASET FOR THE 2019 EVENT	5
S2. SUPPLEMENTARY METHODS	6
S2.1 POROELASTIC REBOUND	7
S2.2 VISCOELASTIC RELAXATION	8
S2.3 OTHER COSEISMIC SLIP MODELS AND SEISMIC VELOCITY STRUCTURES	10
S2.4 AFTERSLIP	11
<i>s2.4.1 Stress-driven afterslip</i>	11
<i>s2.4.2 Kinematic afterslip</i>	12
S2.5 FITTING CRITERION	15
S3. SUPPLEMENTARY RESULTS	15
S3.1 POROELASTIC REBOUND	15
S3.2 UNIVISCOUS LOWER CRUST AND BIVISCOUS UPPER MANTLE	17
S3.3 BIVISCOUS LOWER CRUST AND UPPER MANTLE	18
S3.4 TRANSIENT RHEOLOGY INFERRED FROM POST-RIDGECREST GPS MEASUREMENTS	20
S4. SUPPLEMENTARY TABLE	22
TABLE DR1 MISFIT TO THE DATA	22
FIGURE CAPTIONS	23
REFERENCES	40

S1. Supplementary Data

S1.1 A unified postseismic GPS position time series dataset for the 1992 and 1999 events

We consider GPS measurements within 300 km from the epicentral area of the two Mojave earthquakes, spanning the 1992-2010.26 period (until 4 April 2010 Mw7.2 El Mayor-Cucapah earthquake). We do not consider the post-El Mayor-Cucapah GPS data in the Mojave region, because postseismic transients of the 2010 event have disturbed those data (Dickinson-Lovell et al., 2017).

The spatial and temporal coverage of GPS measurements have improved dramatically as the GPS networks expanded, in particular since 2000. The continuous GPS (cGPS) sites initially belong to the Southern California Integrated GPS Network (SCIGN, <http://sceinfo.usc.edu/education/k12/learn/scign1.htm>) and later the Plate Boundary Observatory GPS network (<http://pboweb.unavco.org>). To monitor postseismic deformation of the 1992 Landers earthquake, the U.S. Geological Survey established a GPS profile (the USGS Emerson transect) consisting of 10 campaign GPS sites across the Emerson fault (Savage and Svarc, 1997).

Several groups have focused on and processed different subsets of the data (Shen et al., 2011). Here, we use GPS time series from the Geodesy Group of the Southern California Earthquake Center (CMM4, Crustal Motion Map Version 4) (Shen et al., 2011) and from the Nevada Geodetic Lab (NGL, geodesy.unr.edu/gps_timeseries/tenv/NA12/, access date: 27 March, 2020). The CMM4 GPS data are mainly derived from 1992-2004 campaign GPS measurements in Southern California (Figures DR1-DR2). The NGL GPS dataset includes additional data from stations in the Yucca Mountain region and is mainly derived from post-Hector Mine continuous GPS observations (Figure DR2).

In this study, the CMM4 (1992-2004) and NGL (1999-2010) datasets are divided into three categories: (1) post-Landers and pre-Hector Mine CMM4 GPS data (GPS stations are shown in Figure DR1a), (2) post-Hector Mine CMM4 near-field campaign GPS data (GPS stations are shown in Figure DR1b), and (3) post-Hector Mine NGL cGPS data (GPS stations are shown in Figure DR1b). The CMM4 GPS data end before 2004.74, and NGL GPS data are post-Hector Mine observations up to the April 4, 2010 Mw 7.4 El Mayor-Cucapah earthquake whose co- and post-seismic deformation extended across the Mojave Desert region. Because postseismic displacements after the 1999 Hector Mine earthquake are consistent at the co-located sites from the CMM4 and NGL solutions, time series from both solutions (CMM4 and NGL) can be combined to extend the time span at several GPS sites (e.g., SDHL). For the other co-located sites, GPS time series with the longer time span (from the NGL solution) are chosen in the subsequent modeling.

s1.1.1 Subsampling NGL GPS time series

We transform the original NGL daily position time series after the first three months into multi-day combination time series by averaging several days' positions. Here, we uniformly set the 1-sigma uncertainties to 2 mm for the horizontal component, which is comparable to those of the CMM4 solution in which time correlated errors have been thoroughly explored. The 1-sigma uncertainties of the vertical component are uniformly set to 4 mm, consistent with the minimum value of the corresponding 1-sigma uncertainties in the CMM4 solution.

s1.1.2 Correcting residual postseismic transients

The difference between the observed position time series and the steady motion at the background rates represents the postseismic relaxation signals. The accuracy of postseismic relaxation time series depends on how well the nominally interseismic GPS velocities represent the background rates. However, the published interseismic velocity fields rely on

how well the apparent postseismic transients are removed from post-earthquake GPS observations. As shown in a previous study that considers preseismic triangulation and trilateration data (Liu et al., 2015), residual postseismic transients are not negligible in the nominally interseismic CMM4 and NGL GPS velocities in the southern Mojave. Thus, we have to correct the interseismic GPS velocities, which would otherwise give us biased postseismic relaxation time series. We use the velocities predicted from a block model constrained by pre-Landers triangulation and trilateration data as well as far-field GPS velocities (Liu et al., 2015) instead of the original CMM4 and NGL GPS velocities in the southern Mojave, and retain the CMM4 and NGL GPS velocities outside the southern Mojave.

GPS velocities in Southern California may have been disturbed by other large historical (e.g., the 1857 Mw 7.9 Fort Tejon and 1872 Mw 7.4 Owens Valley earthquakes) and pre-historical earthquakes (Johnson et al., 2007; Pollitz et al., 2008). The pre-Landers rates may include effectively steady motion associated with the long-term viscoelastic relaxation following these events. As both spatial and temporal deformation gradients from these events are likely very modest across the region, we do not attempt to correct for them.

s1.1.3 Combining GPS time series

The CMM4 and NGL GPS time series at co-located GPS sites can be combined, because (1) the reference frame misalignment between CMM4 and NGL solutions is minor, and (2) postseismic relaxation time series from both solutions are consistent during the common observation period from 1999 to 2004. More specifically, post-Hector Mine CMM4 time series can be used to extend the time span of NGL time series at a few sites (e.g., SDHL) which lack data for the early rapid postseismic transients; for the other co-located cGPS sites, NGL GPS time series are retained which afford us post-Hector Mine postseismic transient until 2010.26.

s1.1.4 New GPS time series

The CMM4 and NGL postseismic position time series, after the interseismic velocity correction (Liu et al., 2015), feature enduring late-stage postseismic transients after 2006 in the epicentral area of the two Mojave earthquakes (Figure DR2). The major patterns are consistent with a solution which is based on a suite of postseismic deformation models (Pollitz, 2015), but ours are better because of the use of pre-Landers data. The GPS data used in most previous studies, however, suggest that the late-stage postseismic transients were possibly complete by 2006 (Herbert et al., 2014). In our new solution, post-Landers postseismic deformation is still active after 1999 and hence the post-Hector Mine time series describe postseismic deformation associated with both earthquakes. This can be clearly seen by a transition from northward to southward postseismic motions at the sites located in between the coseismic ruptures (AGMT, HCMN, TROY, OPRD, OPCL, and SDHL), after 2006-2007.

s1.2 Postseismic GPS position time series dataset for the 2019

event

The Ridgecrest earthquake sequence primarily consists of a Mw7.1 right-lateral strike-slip faulting on a NW-SE striking fault on 5 July 2019 preceded by a Mw6.4 left-lateral strike-slip faulting on a NE-SW striking fault on 4 July 2019. The epicentral area belongs to the central ECSZ north of the Garlock fault, ~180 km northwest of the epicentral areas of the 1992 and 1999 Mojave earthquakes in the southern ECSZ (Mojave ECSZ).

Here we consider the first year post-Ridgecrest GPS time series from the Nevada Geodetic Lab (geodesy.unr.edu/gps_timeseries/tenv/NA12/, access date: 11 August, 2020) and Scripps Orbit and Permanent Array Center (SOPAC, <ftp://sopac-ftp.ucsd.edu/pub/timeseries/measures/ats/WesternNorthAmerica>, access date: 11 August,

2020) to gain estimates of the transient viscosity of the upper mantle. Because an accurate estimate of the transient viscosity requires well-processed GPS data (beyond the near field), our estimate that relies on preliminarily processed data is not highly precise, but it allows us to make a distinction between the order-of-magnitude difference, for example, 10^{17} Pa s, 10^{18} Pa s, and 10^{19} Pa s. Consequently, this test also enables us to explore the consistency of the transient rheology of the upper mantle beneath the central and southern ECSZ.

s2. Supplementary Methods

Coseismic faulting alters the stress field in the crust and upper mantle. The earthquake-induced stress dissipates with time as several physical processes, such as afterslip, poroelastic rebound, and viscoelastic relaxation, occur in response to the stress redistribution, resulting in time-dependent and observable surface deformation. Both the near-field and far-field GPS observations are influenced by viscoelastic relaxation in the upper mantle (Freed et al., 2007; Pollitz, 2015). The near-field GPS signals include additional contributions from shallower deformation processes, including afterslip (Shen et al., 1994; Savage and Svarc, 1997; Pollitz, 2015), poroelastic rebound (Peltzer et al., 1998; Fialko, 2004a), and viscoelastic relaxation in the lower crust (Deng et al., 1998). We therefore have to explore the relative importance of afterslip, poroelastic rebound, and viscoelastic relaxation when interpreting the post-earthquake GPS observations.

We use layered half-space coseismic slip models of the Landers (Fialko, 2004b) and Hector Mine (Simons et al., 2002) earthquakes as the sources that drive both poroelastic rebound in the crust and active postseismic viscoelastic flow in the viscoelastic substrate. We reduce the deep slip at 10-15 km depth in Fialko's model by 30%, because the coseismic slip solution could include a portion of early afterslip, due to delayed GPS and InSAR measurements recorded after the quake and used to constrain the coseismic slip model. The patterns of the estimated deep slip >2 m along the 60 km long main rupture are also less

reliable owing to the low resolution of slip at depth. For the modified slip model, the deep slip peaks at ~ 4.4 m, and most deep patches have slip < 2 m. The slip model still fits well the GPS-observed coseismic displacements, especially those in the intermediate field (Figure DR3), suggesting that our modification does not omit too much the coseismic stress change in the lower crust which affects the postseismic deformation modeling results. Based on this model, the inferred lower crustal steady-state viscosity is $\sim 8.0 \times 10^{19}$ Pa s when only viscoelastic relaxation (Burgers rheology) is considered, but it increases to $\sim 2 \times 10^{20}$ Pa s when both stress-driven afterslip and viscoelastic relaxation are considered. We also test other scenarios by allowing more reduction of the deep slip (e.g., reducing 50%). The modified model systematically underestimates the intermediate-field coseismic displacements by $\sim 20\%$, and is therefore not adopted.

To ensure consistency, we use the seismic velocity structure model of the Mojave Desert of Jones and Helmberger (1998)—the same as that used to derive the coseismic slip models (Simons et al., 2002; Fialko, 2004b)—throughout our modeling of kinematic afterslip, poroelastic rebound, and distributed viscoelastic relaxation. To explore how the derived viscosities of the lower crust and upper mantle vary, we also consider other combinations of coseismic slip models and earth structures. For the 2019 Ridgecrest earthquake sequence we use a coseismic slip model constrained by GPS and InSAR (Wang et al., 2020) to drive the viscoelastic relaxation. The seismic velocity model is the same as the one for the Mojave case.

s2.1 Poroelastic rebound

We use the software package PEGRN/PECMP (Wang and Kämpel, 2003) to model the time-dependent fluid flow in the porous upper crust in response to coseismic pressure changes. In this model, some elastic parameters (e.g., bulk modulus of the rock matrix) are determined from the seismic velocity model. The other parameters to be determined are the hydraulic diffusivity (D), Skempton's coefficient (B), and Poisson's ratio under undrained and

drained conditions. The amplitude of deformation is mainly dictated by Poisson's ratio under undrained and drained conditions, similar to the case for the fully relaxed state (Peltzer et al., 1998), and the rate of decay is dictated by the hydraulic diffusivity. In the model implementation, we need to consider the trade-off between the contribution from changes in Poisson's ratios and the depth range of fluid flow (controlled by the depth-dependent hydraulic diffusivity). Typically, the permeability (and hence the hydraulic diffusivity) decreases with depth following a power law and perhaps only the very shallow portion hosts active porous flow at the time scale of our observations, with high permeabilities on the order of 10^{-13} - 10^{-14} m² (Townend and Zoback, 2000; Jónsson et al., 2003). Another end-member case is that the entire upper crust is abundant in pores and inter-connected fluids and hence hosts poroelastic rebound after the coseismic stress loading (Fialko, 2004a).

In our model implementation, for the layer(s) hosting active fluid flow, the Skempton's coefficient (B) is set to 0.6; the undrained and drained Poisson's ratios are 0.31 and 0.27, respectively, consistent with previous studies (Peltzer et al., 1998; Fialko, 2004a); the candidate hydraulic diffusivities (D) are 0.1, 0.5, 1.0, 1.5, 2.0, and 2.5 m²/s; and the end-member depth range of porous flow are 0-2.5 km and 0-16 km, respectively.

s2.2 Viscoelastic relaxation

We use the software package PSGRN/PSCMP (Wang et al., 2006) to model distributed viscoelastic relaxation. Despite geodetic and geophysical evidence of heterogeneous lithosphere beneath Southern California (Pollitz, 2015), for simplicity, we only consider laterally homogeneous models. The layered viscoelastic structures tested in this study have a 16-km-thick elastic layer overlying a 12-km-thick viscoelastic lower crust underlain by a viscoelastic half space (Figure DR4).

We first consider rheological models with Burgers rheology for both the lower crust and upper mantle, because (1) Burgers and Maxwell rheologies macroscopically characterize

creep deformation due to dislocation and diffusion creep, respectively (Bürgmann and Dresen, 2008), (2) dislocation creep may prevail in the entire viscoelastic substrate, (3) Burgers rheology yields non-linear deformation patterns similar to the observed postseismic deformation characterized by rapid exponential decay in the first year and more gradual change afterwards (Pollitz, 2003), and (4) the observed transient deformation in the Yucca Mountain region (250 km away from the epicentral regions) indicates that biviscous (e.g., Burgers) or stress-dependent rheology must be considered for the upper mantle (Freed et al., 2012). However, linear diffusion creep may also occur, and therefore we also consider the case with Maxwell rheology for the lower crust and Burgers rheology for the upper mantle. For comparison, we also consider the simplest case with Maxwell rheology for both layers.

For the Burgers rheology in our models, the steady-state shear modulus μ_{MB} and bulk modulus k are determined from the previously established layered P-wave velocity, S-wave velocity, and density (Figure DR4). The yet-to-be-determined parameters are the transient shear modulus μ_{KB} , transient viscosity η_{KB} , and steady-state viscosities η_{MB} of the Burgers body. To reduce the number of unknown parameters (considering the resolving power of GPS data), we fix some of the parameters and only explore the steady-state viscosities of the Burgers body (η_{MB}) using a grid search. The ratio of the transient viscosity to the steady-state viscosity ($\eta_{\text{KB}}/\eta_{\text{MB}}$) is fixed at 0.1, consistent with previous studies (Freed et al., 2012; Pollitz, 2015). We also test other values of $\eta_{\text{KB}}/\eta_{\text{MB}}$ less than 0.1 (e.g., 0.02, 0.05, and 0.075). We find that the estimates of the steady-state viscosities (η_{MB}) are not sensitive to $\eta_{\text{KB}}/\eta_{\text{MB}}$ if $\eta_{\text{KB}}/\eta_{\text{MB}}$ is less than or equal to 0.1. We find that $\eta_{\text{KB}}/\eta_{\text{MB}}$ should be 0.1 for the upper mantle, otherwise the models fit the far-field data worse. We also find that the preferred $\eta_{\text{KB}}/\eta_{\text{MB}}$ is smaller than 0.1 but greater than 0.02 (e.g., 0.05) when only viscoelastic relaxation is considered for modeling the near-field data. To estimate the effects of transient rheology, we also consider the models constrained by GPS time series in different time periods (the first 1

month, 1 year, and the full 18 years for the Mojave case; the first 1 month and 1 year for the Ridgecrest case.). The ratio of the fully relaxed shear modulus ($\mu_{MB}\mu_{KB}/(\mu_{MB}+\mu_{KB})$) to unrelaxed shear modulus (μ_{MB}), parameterized by a in PSGRN, also influences the amount of early rapid transient deformation. We examine a between 0.1 and 0.9 in 0.1 increment (the optimal a is ~ 0.7).

Because the chosen viscoelastic rheology is linear, the modeled viscoelastic relaxation for both earthquakes can be summed up. However, if power-law rheology applies, the effective viscosity is stress-dependent, and the post-Landers GPS-derived viscosities would differ from those from post-Hector Mine GPS data. Our modeling results show that the rheological structures constrained separately by the post-Landers and post-Hector Mine data are slightly different but consistent, which suggests that the earthquake-induced stress changes are not significantly larger than the background stress. This is an open question that should be further addressed in follow-up studies.

s2.3 Other coseismic slip models and seismic velocity structures

How the estimates of the effective viscosities of the lower crust and upper mantle vary is mainly dictated by the patterns and magnitudes of deviatoric stress change induced by the coseismic rupture, which is determined by the choice of coseismic slip model and seismic velocity model. For that reason, we also consider the coseismic slip models in homogeneous half-space earth model (Wald and Heaton, 1994; Jónsson et al., 2002) and other seismic velocity models such as the one used in Pollitz's previous studies (Pollitz, 2003, 2015) and the 1D seismic velocity model (Figure DR4) for the Mojave region that is derived from the 3D SCEC Southern California Community Velocity Model Version 4 (SCEC CVM4, <http://scedc.caltech.edu/research-tools/3d-velocity.html>). The coseismic slip models in layered half-space earth model have $\sim 20\%$ larger deep slip than those in homogeneous half-space earth model. The excess of slip at depth for the coseismic slip models in the layered

earth model provides a greater deviatoric stress change to drive viscoelastic relaxation in the lower crust and upper mantle (we find that the choices of coseismic slip models do matter for modeling the near- and intermediate-field post-Landers and post-Hector Mine deformation field due to viscoelastic relaxation). The shear modulus of the 1D CVM4 agrees with that of the model used in Pollitz’s previous studies (Pollitz, 2003, 2015), except for a difference less than 15% in the upper crust (<16 km depth, Figure DR4); the shear modulus of the lower crust is ~19% greater than that of the JH1998 model for the Mojave region. To test the effects of the choice of coseismic slip model and seismic velocity model, we use the post-Landers and post-Hector Mine GPS data to constrain the viscoelastic relaxation models. First, we test the case based on coseismic slip models in layered half-space earth model and the JH1998 earth structure, which serves as the reference case. Second, we test the case based on the coseismic slip models in layered half-space earth model and 1D CVM4 earth structure. When compared to the results of the reference case, the estimated viscosities of the lower crust increase by a factor of ~1.5, but the viscosities of upper mantle retain at approximately the same level. Third, we test the case based on the coseismic slip models in homogeneous half-space earth model and 1D CVM4 earth model. When compared to the reference results, the estimated viscosities of the lower crust decrease by a factor of 1.0-1.5, but the viscosities of upper mantle retain at approximately the same level.

s2.4 Afterslip

s2.4.1 Stress-driven afterslip

We consider stress-driven deep afterslip at 16-34 km depth that is simulated using the software package Unicycle (Barbot et al., 2009; Barbot et al., 2017). Rate-strengthening friction applies and the initial slip velocity, V , is determined by

$$V = 2V_0 \sinh(\Delta\tau/a\sigma)$$

(s1)

in which V_0 is a reference velocity, $\Delta\tau$ is coseismic shear stress change, σ is effective normal stress, and a is the friction parameter. We test V_0 in the range 10^{-4} - 10^0 m/yr and a in the range 10^{-5} - 10^0 . The data constraints are the residual time series from the viscoelastic relaxation modeling, with steady-state viscosities allowed to range from 1×10^{18} to 1×10^{22} Pa s.

Stress-driven afterslip is dictated by the coseismic stress change and the two free model parameters V_0 and $a\sigma$, thus the number of free parameters is usually much less than that of kinematic afterslip models (see Table DR1). Therefore, stress-driven afterslip models generally fit the data worse than the kinematic afterslip model. However, kinematic afterslip models are often physically implausible because the distribution of afterslip is not related to the available stress change. In this study, our preferred combined model is the joint inversion of stress-driven afterslip and viscoelastic relaxation.

s2.4.2 Kinematic afterslip

We also estimate the distribution of afterslip on and below the coseismic rupture plane(s) following a kinematic slip inversion approach. The kinematic slip model serves as independent references to our stress-driven afterslip model. In the kinematic afterslip inversion, the observed data \mathbf{d} are related to afterslip \mathbf{s} by Green's functions \mathbf{G} for rectangular dislocations in a layered half-space (Wang et al., 2003). To regularize the inversion problem, the second order Laplacian operator \mathbf{L} is applied to smooth the afterslip distribution. These can be represented by the following equation

$$\begin{aligned} \mathbf{d} &= \mathbf{G}\mathbf{s} + \boldsymbol{\varepsilon} \\ \mathbf{0} &= \mathbf{L}\mathbf{s} + \mathbf{e} \end{aligned}$$

(s2)

where $\boldsymbol{\varepsilon}$ denotes data errors that are assumed to follow a Gaussian distribution, \mathbf{e} characterizes the uncertainties applied to the smoothing constraints (equivalent to pseudo-observations) that are uniformly set by λ . The trade-off between data misfit and roughness of

the afterslip should be explored in this optimization, which is determined by choosing an optimal λ from the data misfit versus model roughness curve.

We subtract viscoelastic response (as described in the Section s3.2-3.4) from the GPS position time series, fit the residual time series by logarithmic function (characteristic times are 10 days for both the post-Landers and post-Hector Mine data), obtain the 5-year cumulative displacements, and invert the cumulative displacements for the distribution of afterslip. We choose the time span of post-Hector Mine CMM4 GPS measurements—5 years—as the time window for afterslip inversion. How we set the characteristic time of the logarithmic function affects the estimates of steady-state viscosities of the lower crust and upper mantle. We will discuss this issue in joint inversion of afterslip and viscoelastic relaxation in the subsequent sections.

For the afterslip model of the 1992 Landers earthquake, the fault geometry at 0-34 km depth is discretized into 884 3×2 km rectangular patches. For the 1999 Hector Mine earthquake, we estimate afterslip on 1164 3×1.5 km rectangular patches at 0-34 km depth.

The post-Landers GPS data is influenced by afterslip related to the 1992 event. Therefore, we invert the 1992-1997 cumulative displacements (based on the residual time series as mentioned before) for the distribution of afterslip on and below the 1992 rupture. The post-Hector Mine GPS data is not only influenced by afterslip related to the 1999 event but also by potential afterslip related to the 1992 event. Therefore, we invert the 1999-2005 cumulative displacements, with correction for the contribution from the 1992 Landers afterslip models, for the distribution of afterslip on and below the 1999 rupture.

We first invert separately the post-Landers (but pre-Hector Mine) and post-Hector Mine data for the distribution of afterslip for the 1992 and 1999 events, respectively. However, given that both the post-Landers (pre-Hector Mine) and post-Hector Mine data

have limitations in spatial and temporal coverage, we also use all the data to constrain the distribution of afterslip for both events.

How well the afterslip is resolved by the available GPS data? To address this issue, we invert the 5-year cumulative displacements (derived from the residual time series) for the distribution of afterslip, using least square method, and we check the trade-off between the resolution and data misfit. No matter how the rheology is used (Maxwell or Burgers rheology) to model the contribution from viscoelastic relaxation, the sums of diagonal terms of the resolution matrix are ~ 15 for afterslip inversion of both the 1992 and 1999 events, when the data is modestly fitted by the models (based on the trade-off curves). When compared to the number of fault patches (884 and 1164 for the 1992 and 1999 events, respectively), the values of the sums of diagonal terms of the resolution matrix being ~ 15 suggest that patterns of afterslip distributed over large region are reliable (perhaps at dimension of $\sim 20 \times 10$ km for the deep afterslip).

We impose positivity constraint to get right-lateral slip in afterslip inversion. When the viscosities of the viscoelastic layers are small such that the model predicted fault-parallel motion from viscoelastic relaxation exceed the observed magnitudes, the residual time series (observed minus modeled) require left-lateral slip, which does not make sense. In that case, afterslip is not allowed to occur. For the other cases, however, right-lateral afterslip is required to fit the data. We choose the extent of smoothing constraint applied in the inversion by examining the trade-off curves between slip roughness and data misfit. According to the trade-off curve, a unified value of the smoothing parameter can be used in all the joint inversions. When the smoothing parameter varies around the optimized value, the inferred viscosities almost do not change, but the magnitude of peak afterslip may change a bit (e.g., when λ doubles, the estimated afterslip is rougher, with peak slip increasing by less than 100%, but the estimated viscosities remains at approximately the same values).

s2.5 Fitting criterion

We choose the best-fit models that minimize weighted residual sum of squares (WRSS) of the GPS position time series:

$$WRSS = \sum_{i=1}^2 \sum_{j=1}^{Ns} \sum_{k=1}^{Nt} [(d_{ijk}^o - d_{ijk}^m - d_{ij}^c) / \sigma_{ijk}]^2$$

(s3)

where the summation is over Ns stations ($j=1, Ns$) whose east-west ($i=1$) and north-south ($i=2$) components have Nt epochs of data ($k=1, Nt$, each station has a different Nt), d_{ijk}^o and d_{ijk}^m are the observed and modeled displacements, respectively, σ_{ijk} is the 1-sigma uncertainty, and d_{ij}^c is the offset to align d_{ijk}^o with d_{ijk}^m that is estimated from the misalignments ($d_{ijk}^o - d_{ijk}^m$) by least-squares. As an alternative to estimating d_{ij}^c from $d_{ijk}^o - d_{ijk}^m$, we estimate d_{ij}^c from d_{ijk}^o , which compulsively align d_{ijk}^m with d_{ijk}^o in the early period; the resultant overall data misfit is worse (increasing WRSS by a factor of ~ 4) and the estimates of viscosities of the lower crust decrease by a factor of 1.0-1.3.

s3. Supplementary Results

s3.1 Poroelastic rebound

Are the signals induced by poroelastic rebound discernable by post-Landers campaign GPS and post-Hector Mine cGPS measurements? To address this issue, we first obtain the best-fit viscoelastic relaxation and stress-driven afterslip models and then test whether the addition of poroelastic rebound helps to reduce the data misfit (both horizontal and vertical components). We test two scenarios of poroelastic rebound (Figure DR5A): (1) one in the shallow 2.5 km of the upper crust and (2) the other one throughout the upper crust (0-16 km).

First, we test the model whether the inclusion of poroelastic rebound reduce the misfit to horizontal component of data. When poroelastic rebound and the viscoelastic relaxation

model with Burgers rheology are used to fit the data, we find that the scenario (1) (blue circles in Figure DR5B) fit the data better than the scenario (2) (red circles in Figure DR5B). We also find that the scenario (1) may help to reduce the data misfit of the models with only viscoelastic relaxation (data misfit is shown by the green line in Figure DR5B), if the hydraulic diffusivity is greater than $0.5 \text{ m}^2/\text{s}$. For the scenario (2), the predicted deformation is distributed more than 20 km from the coseismic rupture (Figure DR5A), and although the predicted fault-perpendicular motion can be used to remedy model misfit (due to viscoelastic relaxation) to the observed fault-perpendicular motion, the predicted fault-parallel motion will deteriorate the model fit to the data. When the viscoelastic relaxation model with Maxwell rheology is first used to fit the data, the addition of poroelastic rebound does reduce the data misfit (dashed green line versus red and blue squares in Figure DR5B-5C).

The addition of shallow poroelastic rebound also helps to explain the observed vertical deformation in the first two years following the 1992 (Figure DR6) and 1999 (Figure 3 in the main text) events. The optimal stress-driven afterslip and viscoelastic relaxation model cannot give a perfect match to the observed vertical deformation within ~ 10 km from the fault (Figure 3D and Figure DR6D). The spatial patterns of the mismatch are opposite to model predictions of shallow poroelastic rebound (Figure 4A and Figure DR6A). When combined with additional contribution from shallow poroelastic rebound, the combined mode fits the post-Landers CMM4 campaign GPS and post-Hector Mine cGPS data better at the 99.9% and 89.4% confidence level. Therefore, consideration of shallow poroelastic rebound, stress-driven afterslip, and viscoelastic relaxation can explain the spatial patterns of the observed vertical deformation (Figure 4E and Figure DR6E). Note that the major patterns of the modeled shallow poroelastic rebound do not vary (Figure DR7), even though coseismic slip models with better resolution on the distribution of shallow slip are considered (Xu et al., 2016).

How the poroelastic rebound-induced deformation decays with time is mainly dictated by hydraulic diffusivity. We examine the case with poroelastic rebound and the viscoelastic relaxation model with Burgers rheology. We test several candidate values of hydraulic diffusivity: 0.1, 0.5, 1.0, 1.5, 2.0, and 2.5 m²/s. For the cases with poroelastic rebound in the shallow 2.5 km, the goodness of fit is best when hydraulic diffusivity is ~2.5 m²/s, but the data misfit is essentially equivalent when the hydraulic diffusivity varies from 1.0 m²/s to 2.5 m²/s (blue squares in Figure DR5C).

In summary, GPS measurements, although sparsely distributed, support shallow poroelastic rebound, rather than the upper crustal scale poroelastic rebound (Fialko, 2004a), for the Mojave case. InSAR data with better spatial coverage along the 1992 and 1999 ruptures (in particular the stepovers) is required for a better understanding of how poroelastic rebound developed after the two earthquakes. The following models with viscoelastic relaxation include a contribution from poroelastic rebound in the upper 2.5 km with a hydraulic diffusivity of 1.0 m²/s. However, the viscosity estimates are not sensitive to whether the shallow poroelastic rebound is considered.

s3.2 Univiscous lower crust and biviscous upper mantle

We consider the cases with Maxwell rheology for the lower crust and Burgers rheology for the upper mantle (the ratio of the transient viscosity to the steady-state viscosity is fixed at 0.1), because (1) the microscale physical processes responsible for ductile deformation may be diffusion creep and dislocation creep for the lower crust and upper mantle, respectively, and (2) the observed transient deformation in the Yucca Mountain region (250 km away from the epicentral regions) support biviscous (e.g., Burgers) or stress-dependent rheology for the upper mantle (Freed et al., 2012).

The steady-state viscosity of the lower crust can be $\sim 1.0 \times 10^{20}$ Pa s, less than three times that of the upper mantle, in a joint inversion of both kinematic/stress-driven afterslip

and viscoelastic relaxation (Figure DR8 and Table DR1). The estimated stress-driven afterslip lasts for more than 4 years and does not exhibit rapid early transients within the first year (Figure DR9). The best-fit models fit all the 18-years GPS data worse than the corresponding best-fit models with Burgers rheology for the lower crust (see Section s3.3) at the 99% confidence level.

We also test the effects of the ratio of the transient viscosity to the steady-state viscosity (Burgers rheology for the upper mantle). When that ratio is less than 0.1 (e.g., 0.02, 0.05, and 0.075), the best-fit models with only viscoelastic relaxation fit the data (both the near-field and far-field data, in particular, the far-field data) worse than the best-fit model with that ratio being 0.1. The data do not allow us to make a distinction between the models with that ratio being 0.1 and 0.075, because data misfits are statistically comparable at the 55.55% confidence level. However, the models with that ratio ≤ 0.05 fit the data worse than the model with that ratio being 0.1 at $>95.00\%$ confidence level. Note that the estimates of the steady-state viscosity are not sensitive to the tested ratios of the transient viscosity to the steady-state viscosity (similar conclusions apply to the Section S3.3).

s3.3 Biviscous lower crust and upper mantle

We consider the cases with Burgers rheology (the ratio of the transient viscosity to the steady-state viscosity is fixed at 0.1) for both the lower crust and upper mantle, because dislocation creep might occur in both layers. The rheological parameters are presented in the Table DR1. Shown in Figure DR10 is misfit to GPS data in the time period 1992-1999, 1999-2010, and 1992-2010. Shown in Figure DR11 are the distribution of afterslip of the 1992 and 1999 events. Shown in Figure DR6 is the model predicted vertical displacements in the first two years after the 1992 Landers earthquake. Shown in Figures DR12-DR13 are the near-field deformation predicted by the best-fit model with poroelastic rebound and viscoelastic

relaxation. With additional contribution from stress-driven afterslip, the model predictions are shown in Figures DR14-DR15.

When additional contribution from stress-driven afterslip is considered (Figure DR10-DR11), the best-fitting steady-state viscosity of the lower crust is $\sim 2 \times 10^{20}$ Pa s (Table DR1), ~ 5 times of that of the upper mantle. The stress-driven afterslip induces early rapid deformation and ends within the first 3 years (Figures DR14-DR15). Viscoelastic relaxation in the lower crust and upper mantle induce the slowly decaying but long-lasting displacements in the near field.

When additional contribution from kinematic afterslip is considered (Figure DR10-DR11), the steady-state viscosity of the lower crust can be $\sim 9 \times 10^{20}$ Pa s (Table DR1), an order of magnitude larger than that of the upper mantle. That does not indicate that the relaxation of the lower crust has not come into play in the first two decades. We believe that the role of the derived kinematic afterslip is exaggerated and the effects of viscoelastic relaxation in the lower crust are underestimated. That is because: (1) The derived kinematic afterslip lasts for at least one decade (in particular for the afterslip associated with the 1992 event, see Figure DR11) and induces steady-deformation that should be attributed to bulk viscoelastic relaxation. (2) The distribution of afterslip is not dictated by the coseismic stress loading (especially for the kinematic afterslip of the 1999 Hector Mine event, see Figure DR11G).

We also test the effects of the ratio of the transient viscosity to the steady-state viscosity. When that ratio is less than 0.1 (e.g., 0.05 and 0.075) but greater than 0.02, overall, the best-fit models with only viscoelastic relaxation fit the data better than the best-fit model with that ratio being 0.1, at $>94.25\%$ confidence level (The data misfit decreases as that ratio decreases until when the ratio is 0.02. When the ratio is 0.05, the model fit the data better at the 99.47% confidence level.). The relevant models with smaller values of that ratio fit the

near-field data better, but fit the far-field data worse. However, F-test shows that the far-field data misfits are statistically comparable at the <71% confidence level, when that ratios are in the range from 0.05 to 0.1. The transient viscosity of the lower crust constrained by all the 1992-2010 data is estimated to be $\sim 1 \times 10^{19}$ Pa s, less than 4 times that of the upper mantle. The transient viscosity of the lower crust is estimated to be $\sim 1 \times 10^{18}$ Pa s and $\sim 3 \times 10^{18}$ Pa s from the GPS data in the first month and in the first year following the two earthquakes, respectively. These modeling tests, together with other tests in this section, reveal that transient deformation in the lower crust is not negligible after the two Mojave earthquakes.

s3.4 Transient rheology inferred from post-Ridgecrest GPS

measurements

To obtain a first estimate of the transient viscosity of the upper mantle, we first use a coseismic slip model of the Ridgecrest sequence constrained by GPS and InSAR measurement (Kang Wang, personal communications) and our preferred model for the Mojave case (the transient and steady-state viscosities are 4×10^{18} Pa s and 4×10^{19} Pa s for the upper mantle, and 2×10^{19} Pa s and 2×10^{20} Pa s for the lower crust, respectively) to predict the postseismic displacements in the first month. We find that the model predictions are <10% of the observed far-field displacements, suggesting that the transient rheology of the upper mantle is perhaps an order of magnitude smaller. We next adjust the transient and steady-state viscosities of the upper mantle to $3\text{-}5 \times 10^{17}$ Pa s and $3\text{-}5 \times 10^{18}$ Pa s, respectively. The model predictions fit the far-field data well but still underestimate the near-field data by $\sim 20\%$ - 50% (Figure DR16), which suggests (1) that afterslip is required to remedy the near-field data misfit and (2) that the transient viscosity of the upper mantle should be on the order of 10^{17} Pa s in the first year.

To obtain more precise estimates of the transient viscosity, we use the (12-month) post-Ridgecrest GPS time series to constrain viscoelastic relaxation models (Burgers

rheology for both the lower crust and upper mantle; the ratios of the transient viscosity to steady-state viscosity are 0.05 and 0.1). Based on the NGL (SOPAC) dataset, the transient viscosities of the lower crust and upper mantle are estimated to be $1-4 \times 10^{18}$ Pa s ($1-3 \times 10^{18}$ Pa s) and $\sim 4 \times 10^{17}$ Pa s ($\sim 5 \times 10^{17}$ Pa s), respectively. The steady-state viscosities are an order of magnitude larger, but are not well constrained by GPS data spanning less than 1 year. Therefore, we fix the steady-state viscosities at the optimal values derived from the 18-years of GPS data for the Mojave case, assuming that the “long-term” rheological structures should be consistent between the central and southern ECSZ. In that case, the optimal transient viscosity of the upper mantle is $\sim 3 \times 10^{17}$ Pa s constrained by the data in the first month, $\sim 33\%$ of the corresponding value ($\sim 1 \times 10^{18}$ Pa s) constrained by all the data in the first year.

To assess whether the estimates of viscosity for the Ridgecrest case are compatible with those of the Mojave earthquakes, we use 30 days of post-Landers and post-Hector Mine GPS data to constrain viscoelastic relaxation models with Burgers rheology for the upper mantle beneath the Mojave region (the ratios of the transient viscosity to steady-state viscosity are 0.05, 0.075, and 0.1). The transient viscosity of the upper mantle is estimated in the range $\sim 5 \times 10^{17}$ - 1×10^{18} Pa s. When the GPS data in the first year are considered, the transient viscosity of the upper mantle is estimated to be 1×10^{18} - 2×10^{18} Pa s (Burgers rheology) and 3×10^{18} Pa s (If Maxwell rheology is implemented instead, the transient viscosity can be better constrained, because only one parameter is required for each viscoelastic layer). Furthermore, the optimal transient viscosity of the upper mantle is $\sim 4 \times 10^{17}$ Pa s and $\sim 9 \times 10^{17}$ Pa s in the first month and first year, respectively, if the steady-state viscosities are fixed at the optimal values derived from the 18-year GPS data. Some of the previous studies considered primarily near-field GPS and InSAR data within the first 3 years (Pollitz et al., 2001; Pollitz, 2003). Because of insufficient far-field data constraints, the transient viscosity of the upper mantle is not well constrained, but is estimated to be on the

order of 10^{17} Pa s. The data used in our test include more far-field GPS data, which provide robust constraint on the upper mantle rheology. We therefore believe that our estimates of the short-term upper mantle rheology are reliable.

To sum up, based on the data in the first 1 year, the transient rheology of the upper mantle beneath the Ridgecrest region is consistent with that of the upper mantle beneath the southern Mojave. However, because that (1) depth-dependent rheology also gives time-dependent deformation and (2) the estimate of the transient viscosity exhibits a time-dependent pattern (the estimated viscosity increases with time, as the time span of postseismic data lengthens), more and better post-Ridgecrest GPS data are required to obtain conclusive inferences regarding the transient rheology of the upper mantle beneath the Ridgecrest region.

s4. Supplementary Table

Table DR1 | Misfit to the data

Data ^a	Time	Lower crust	a	Viscosity (Pa s)	Upper mantle	a	Viscosity (Pa s)	Misfit (WRSS Chi2) ^b
CMM4	1992-1999	Maxwell	0.0	3.0×10^{19}	Burgers	0.7	3.0×10^{19}	9394.25 3.19 ^c
			0.0	1.0×10^{21}		0.7	3.0×10^{19}	6005.87 2.06 ^d
			0.0	7.0×10^{19}		0.7	2.0×10^{19}	9096.22 3.09 ^e
		Burgers	0.7	6.0×10^{19}	Burgers	0.7	4.0×10^{19}	9232.09 3.14 ^c
			0.7	7.0×10^{20}		0.7	4.0×10^{19}	5555.76 1.91 ^d
			0.7	1.0×10^{20}		0.7	3.0×10^{19}	8987.83 3.06 ^e
NGL	1999-2010	Maxwell	0.0	7.0×10^{19}	Burgers	0.7	3.0×10^{19}	77508.29 1.30
			0.0	1.0×10^{20}		0.7	3.0×10^{19}	69237.24 1.16
			0.0	1.0×10^{20}		0.7	4.0×10^{19}	73600.13 1.24
		Burgers	0.7	8.0×10^{19}	Burgers	0.7	4.0×10^{19}	74336.40 1.25
			0.7	9.0×10^{20}		0.7	4.0×10^{19}	68408.62 1.15
			0.7	4.0×10^{20}		0.7	4.0×10^{19}	72572.18 1.22
CMM4+NGL	1999-2010	Maxwell	0.0	7.0×10^{19}	Burgers	0.7	3.0×10^{19}	79881.34 1.32
			0.0	1.0×10^{20}		0.7	3.0×10^{19}	70985.80 1.17
			0.0	1.0×10^{20}		0.7	4.0×10^{19}	75558.32 1.25
		Burgers	0.7	8.0×10^{19}	Burgers	0.7	4.0×10^{19}	76091.37 1.25
			0.7	9.0×10^{20}		0.7	4.0×10^{19}	69990.63 1.15
			0.7	4.0×10^{20}		0.7	4.0×10^{19}	74440.08 1.23

CMM4 +NGL	1992- 2010	Maxwell	0.0	6.0×10^{19}	Burgers	0.7	3.0×10^{19}	90808.59	1.43
			0.0	1.0×10^{20}		0.7	3.0×10^{19}	77084.00	1.21
			0.0	1.0×10^{20}		0.7	4.0×10^{19}	88727.39	1.39
		Burgers	0.7	8.0×10^{19}	Burgers	0.7	4.0×10^{19}	85390.44	1.34
			0.7	9.0×10^{20}		0.7	4.0×10^{19}	75573.06	1.19
			0.7	2.0×10^{20}		0.7	4.0×10^{19}	84946.31	1.33

a The number of data is 2949, 59515, 60694, and 63643 for the 1992-1999 CMM4, 1999-2010 NGL, 1999-2010 CMM4+NGL, and 1992-2010 CMM4+NGL GPS time series.

b Green and yellow shaded rows indicate the models with the same bulk rheology but constrained by different datasets. Maxwell and Burgers rheologies have 1 and 3 unknown parameters, respectively. Stress-driven afterslip inversion has 2 unknowns. Kinematic afterslip inversion for each event has ~ 15 well-resolved parameters. For the Burgers rheology, the ratio of the transient viscosity to the steady-state viscosity is 0.1.

c Viscoelastic relaxation and shallow poroelastic rebound. The same applies to the first entry of the three entries for each modeling test. So do the second and third entries in **d** and **e**.

d Kinematic afterslip and viscoelastic relaxation (+shallow poroelastic rebound).

e Stress-driven afterslip and viscoelastic relaxation (+shallow poroelastic rebound).

Figure Captions

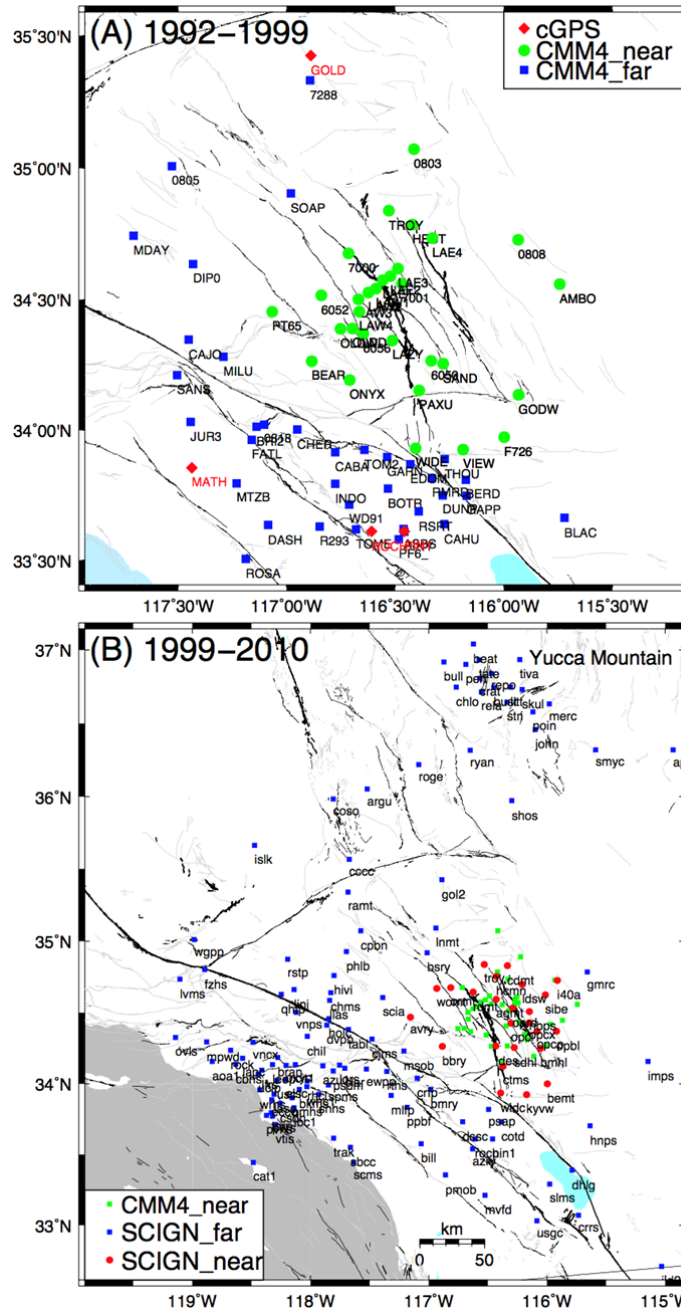


Figure DR1 | Map showing the distribution of (A) post-Landers (1992-1999) and (B) post-Hector Mine (1999-2010) GPS sites. In (A), green circles and blue squares indicate the near- and far-field CMM4 campaign GPS sites, respectively, and red diamonds indicate CMM4 cGPS sites. In (B), red circles, blue squares, and green squares indicate the near-field SCIGN cGPS, far-field SCIGN cGPS, and near-field CMM4 campaign GPS sites, respectively.

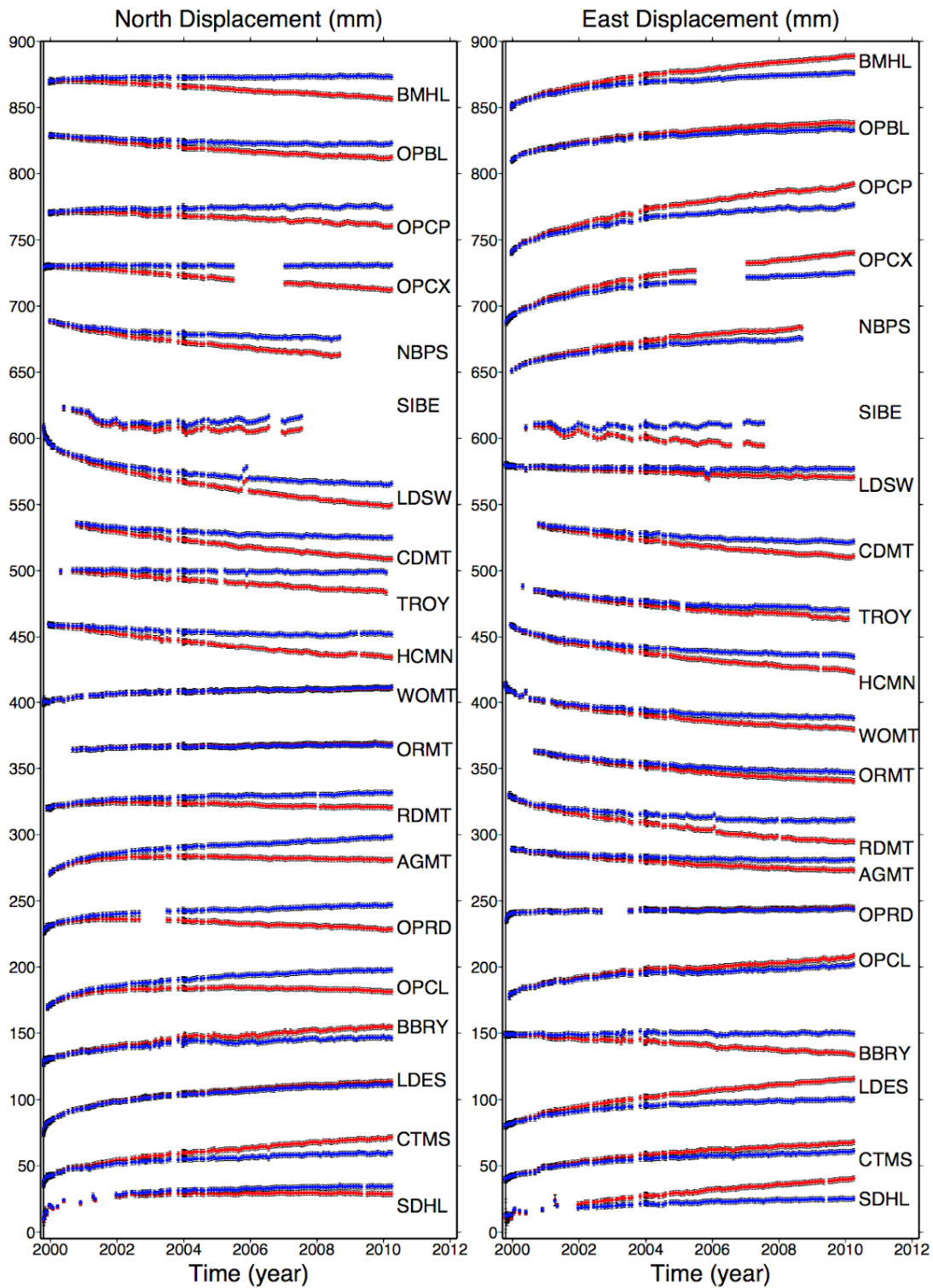


Figure DR2 | Postseismic displacement time series from the NGL solution for SCIGN cGPS sites (1999-2010). The blue dots are the position time series less the originally estimated interseismic motion as described by the NGL velocity estimate. The red dots are based on the new realizations of the secular velocities (Liu et al., 2015).

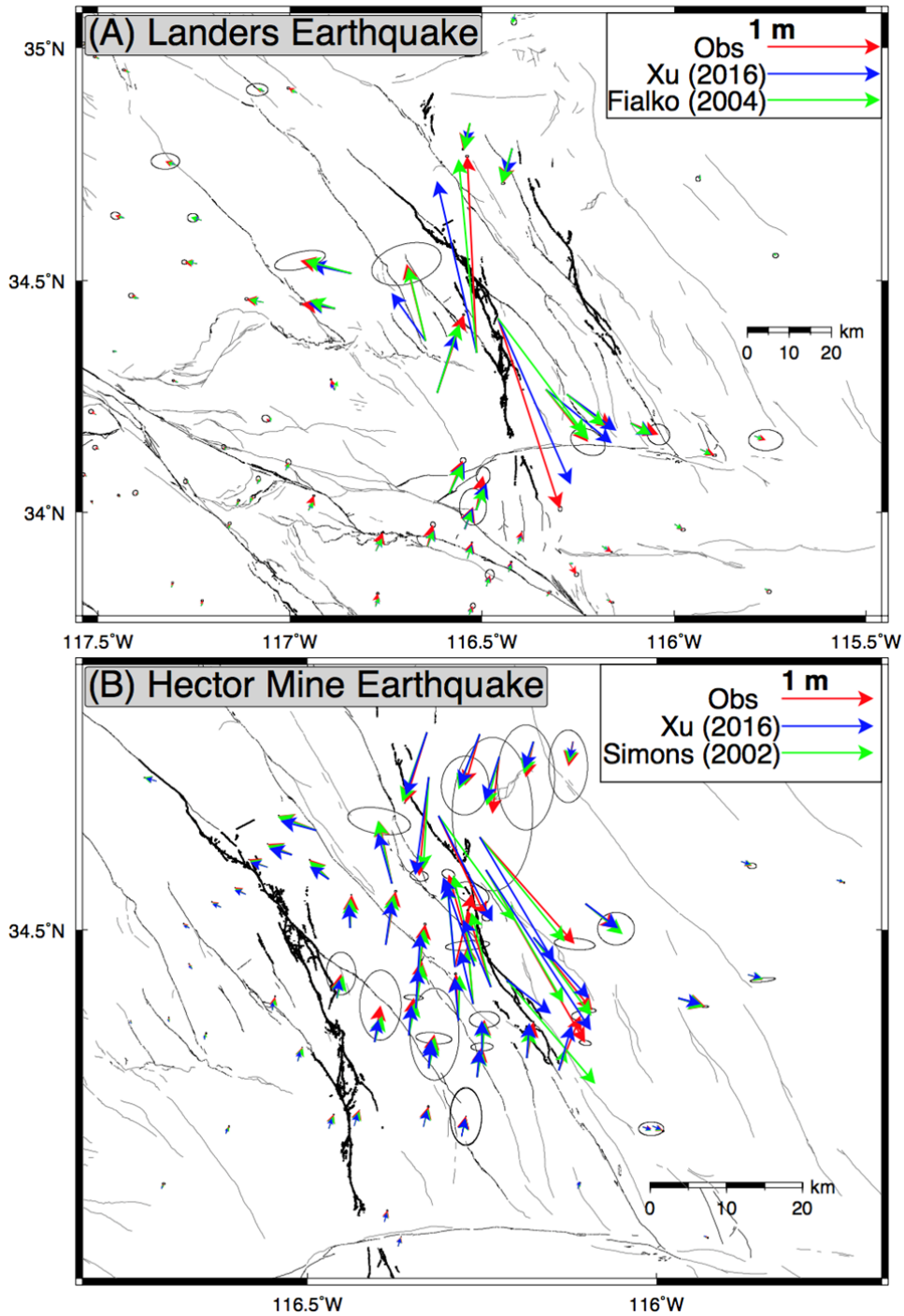


Figure DR3 | Observed and modeled coseismic displacements of the (A) Landers and (B) Hector Mine earthquakes. (A) Red vectors are the observed coseismic displacements; blue and green vectors are the modeled displacements in a layered Earth model, based on coseismic slip model in homogeneous half-space (Xu et al., 2016) and a modified slip model in the same layered Earth model (Fialko, 2004b), respectively. (B) Blue and green vectors are the modeled displacements in a layered Earth model, based on coseismic slip model in homogeneous half-space (Xu et al., 2016) and a modified slip model in the same layered Earth model (Simons et al., 2002), respectively.

Steady-state elastic parameters

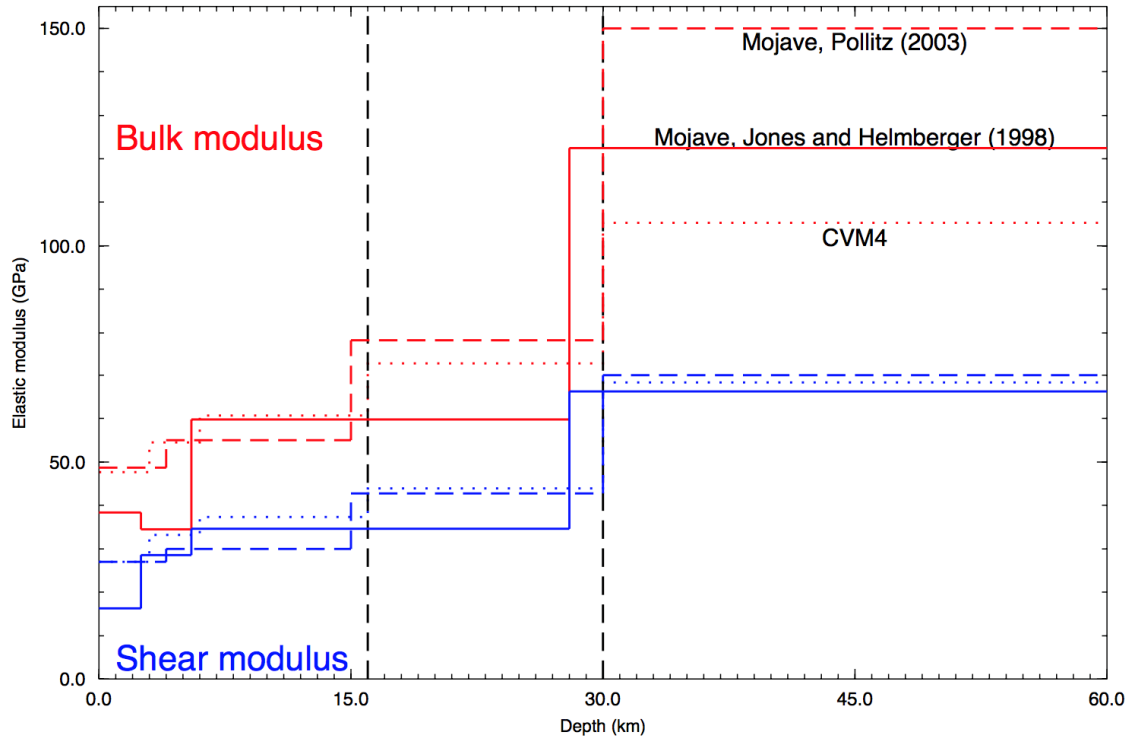


Figure DR4 | Summary of elastic models. Elastic moduli (red and blue lines indicate the bulk and shear modulus, respectively) as a function of depth for JH1998 Mojave (Jones and Helmberger, 1998) (solid lines), CVM4 Mojave (dotted lines), and Pollitz Mojave (Pollitz, 2003, 2015) (dashed lines).

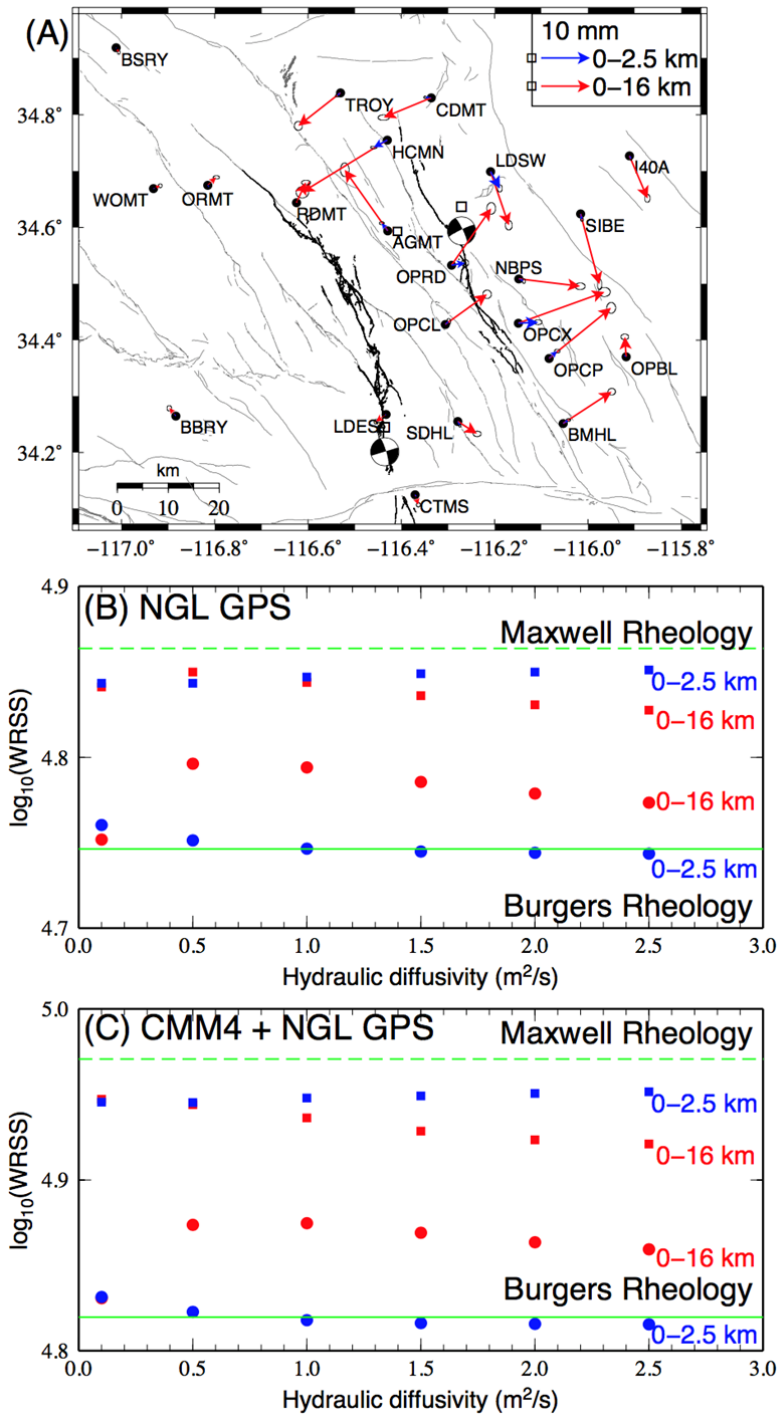


Figure DR5 | (A) Horizontal displacements in the first two years resulting from poroelastic rebound only in the upper 2.5 km (blue vectors) and throughout the entire upper crust (red vectors). (B-C) Data misfit (WRSS, weighted residual sum of squares) to the horizontal component for the (B) NGL GPS and (C) both CMM4 and NGL GPS dataset as a function of hydraulic diffusivity. Green dashed and solid lines indicate the data misfit for the best-fit viscoelastic relaxation model with Maxwell and Burgers rheology, respectively. The squares and circles show how the data misfit for viscoelastic relaxation model with Maxwell and Burgers rheology, respectively, depend on the additional contribution from poroelastic rebound. Blue and red symbols indicate the data misfit when additional contributions from poroelastic rebound at the shallow 0-2.5 km and 0-16 km depths are considered, respectively.

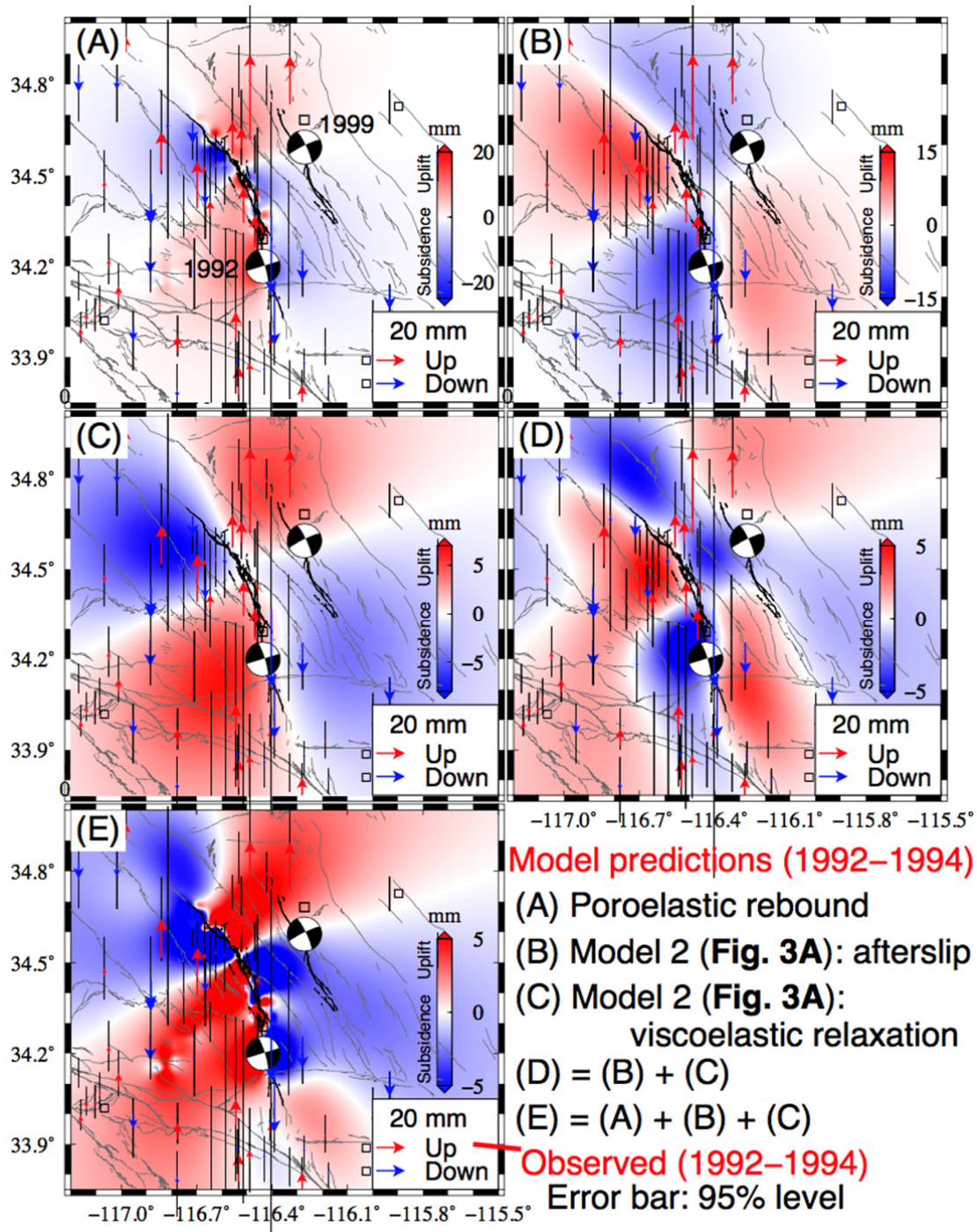


Figure DR6 | Observed and modeled vertical displacements (1992-1994). Color contours are for the modeled vertical deformation field due to (A) shallow poroelastic rebound, (B) stress-driven afterslip, (C) viscoelastic relaxation, (D) the sum of (B) and (C), and (E) sum of the (A), (B), and (C). The vectors are vertical displacements from NGL solution of SCIGN cGPS time series.

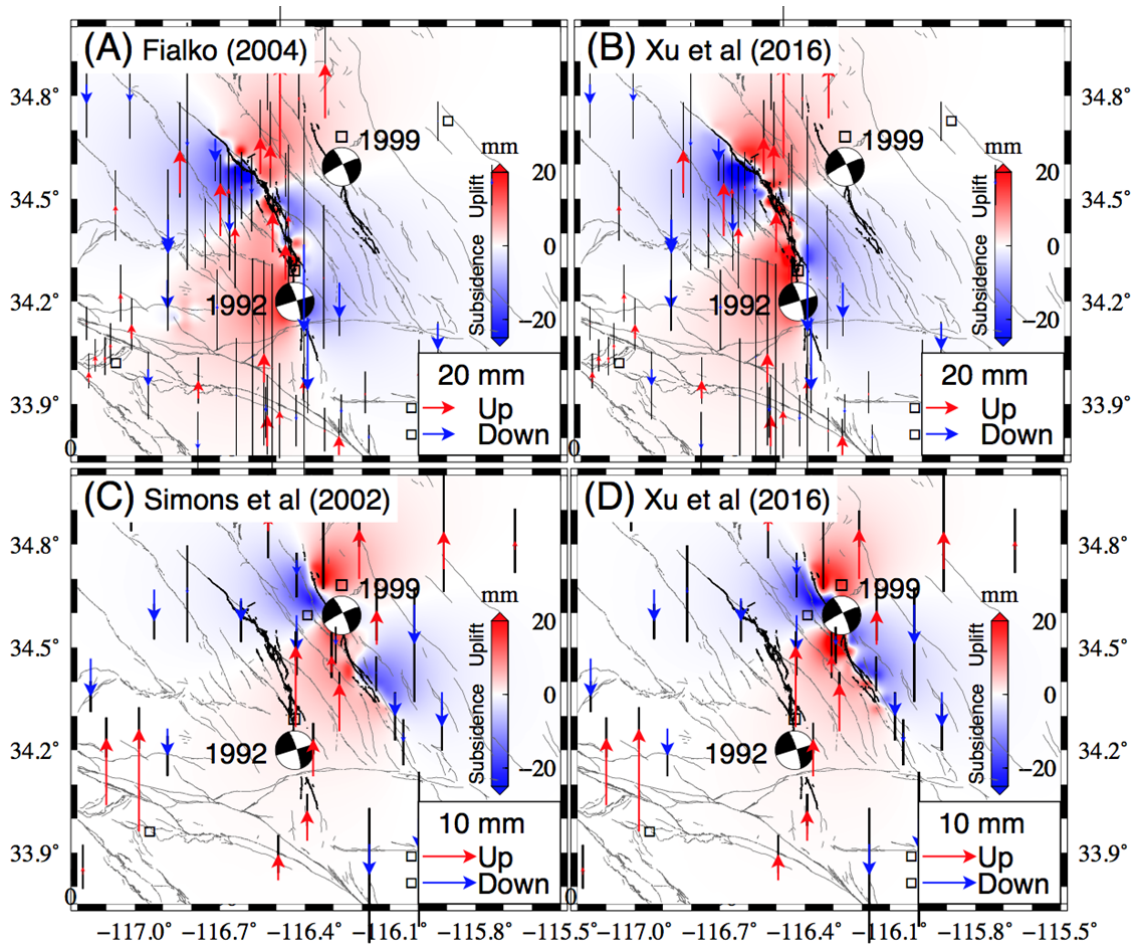


Figure DR7 | Observed and modeled vertical displacements. (A-B): post-Landers in the time period 1992-1994. (C-D): post-Hector Mine in the time period 1999-2002. Model predictions are from shallow poroelastic rebound based on coseismic slip models of (A) Fialko (2004b), (B) Xu et al. (2016), (C) Simons et al. (2002), and (D) Xu et al. (2016).

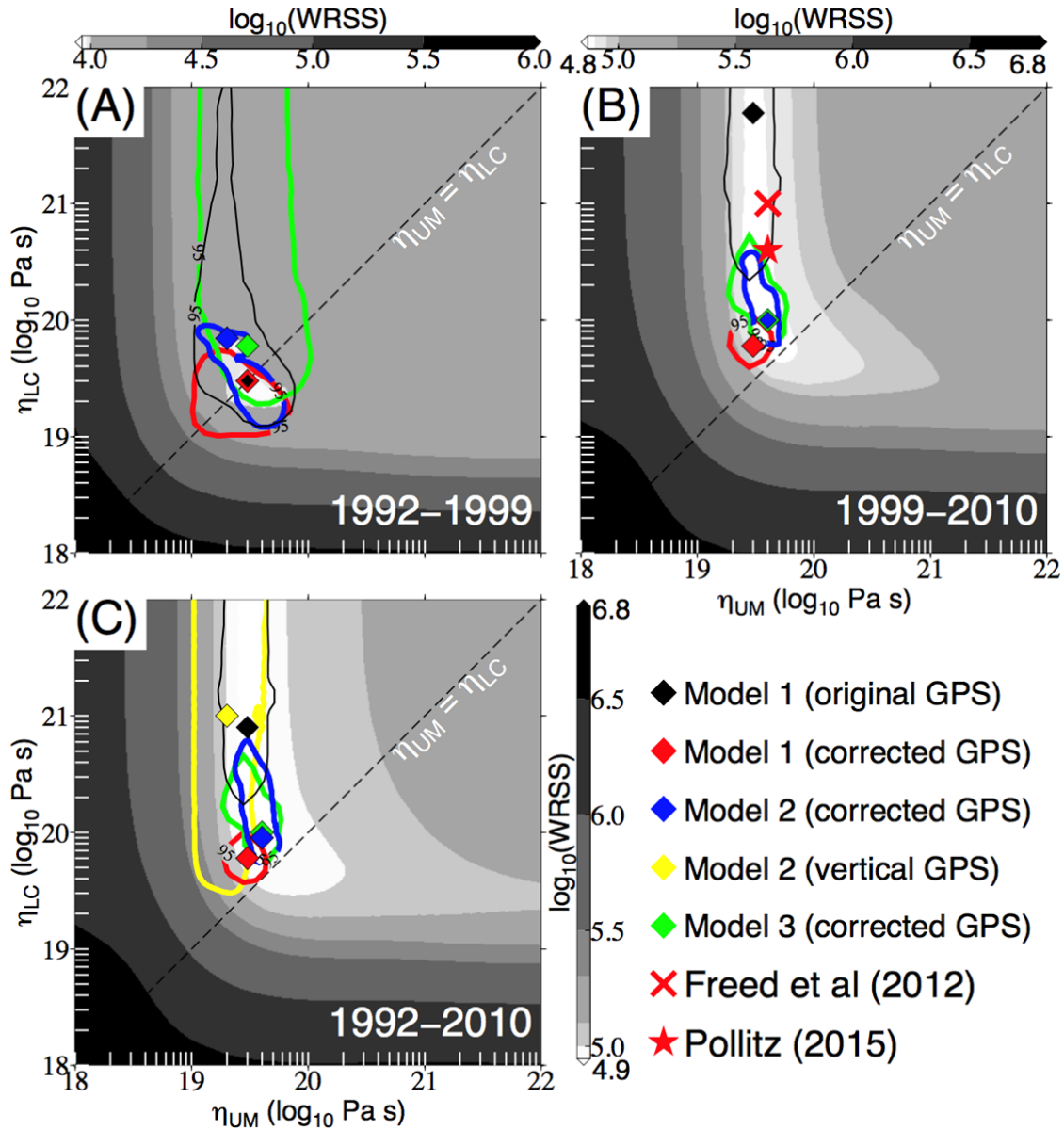


Figure DR8 | Model misfit to data (Maxwell rheology for the lower crust and Burgers rheology for the upper mantle). Data misfit to (A) post-Landers CMM4 GPS, (B) post-Hector Mine GPS, and (C) all the GPS data. Horizontal and vertical axes show the steady-state viscosity of the upper mantle (η_{UM}) and lower crust (η_{LC}), respectively. The colored lines show the statistical 95% confidence regions of the models with respect to the optimal models marked by the color-coded diamonds with only viscoelastic relaxation (Model 1, red contours), with additional contribution from stress-driven afterslip (Model 2, blue contours), and with additional contribution from kinematic afterslip (Model 3, green contours). The yellow diamond and contour are for Model 2 only constrained by vertical GPS data. The black diamond marks the optimal viscosities without afterslip and without considering the interseismic velocity correction (Liu et al., 2015).

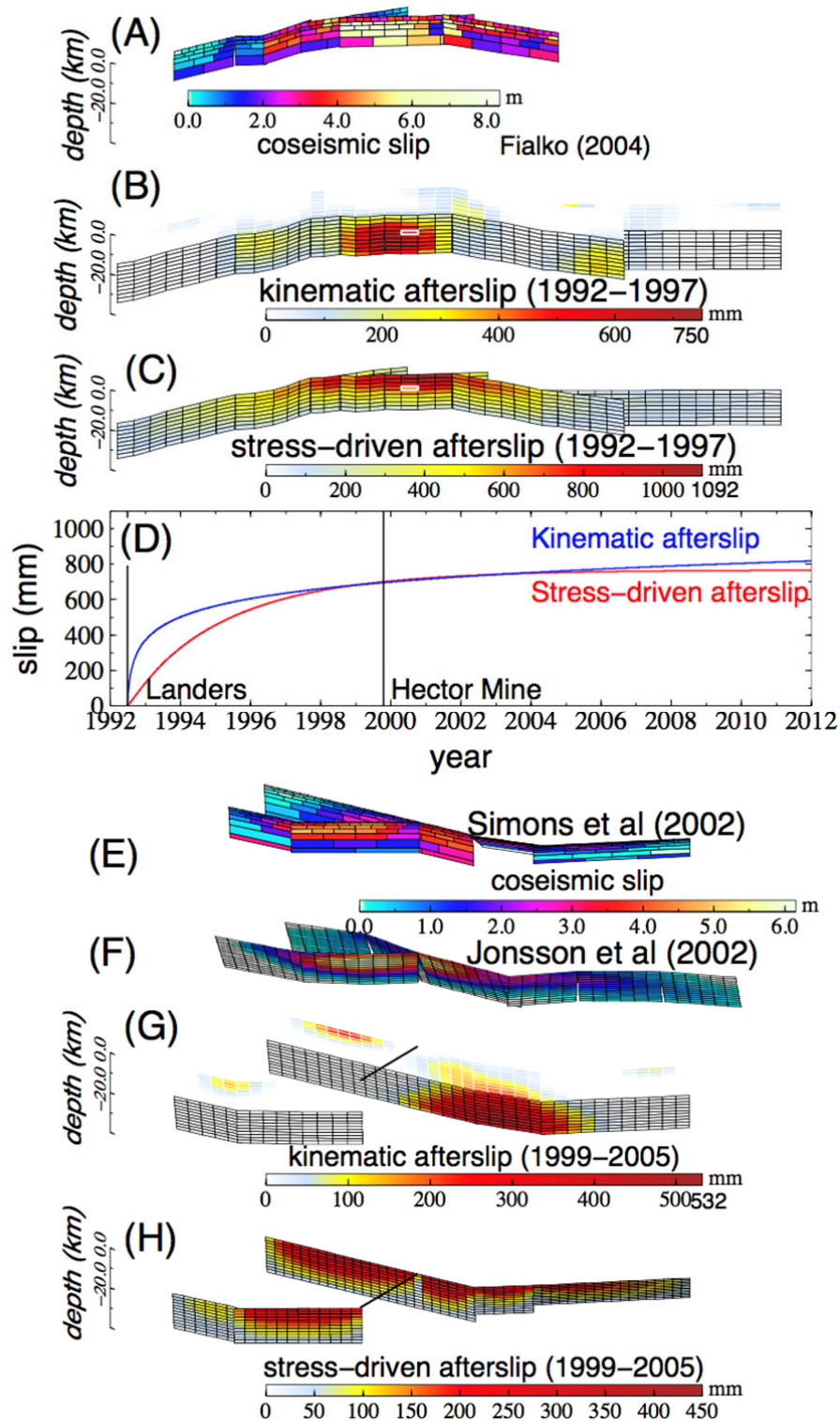


Figure DR9 | Distribution of afterslip for the 1992 Landers and 1999 Hector Mine earthquakes from joint inversion of all the data for afterslip and viscoelastic relaxation (Maxwell rheology for the lower crust and Burgers rheology for the upper mantle). 1992 Landers earthquake: (A) Coseismic slip, (B) Kinematic afterslip (1992–1997), (C) Stress-driven deep afterslip (1992–1997), and (D) temporal evolution of afterslip at the selected patch that is marked by white rectangles in (B) and (C). 1999 Hector Mine earthquake: (E–F) Coseismic slip, (G) Kinematic afterslip (1999–2006), and (H) Stress-driven deep afterslip (1999–2005).

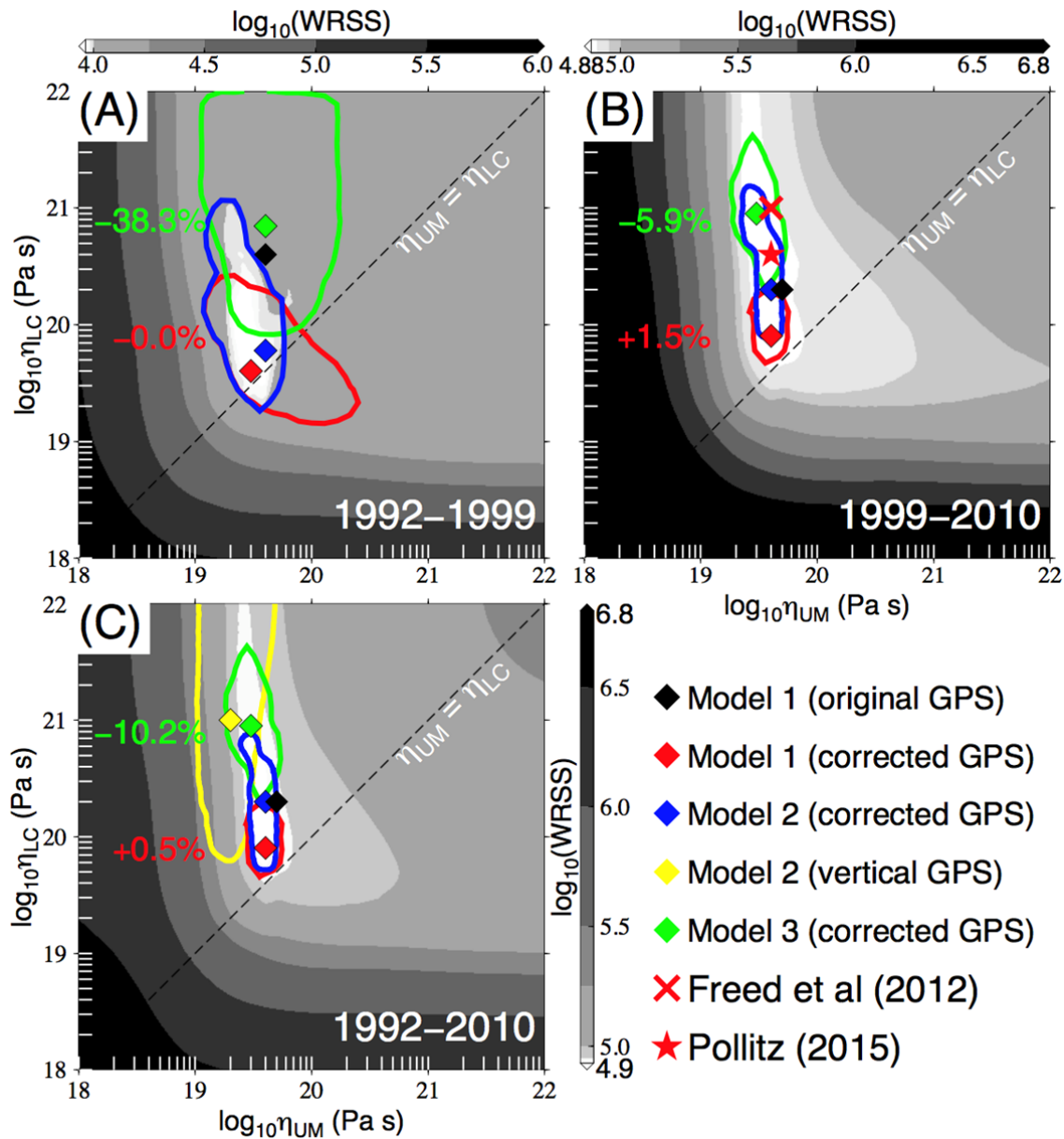


Figure DR10 | Model misfit to data (Burgers rheology for the lower crust and upper mantle). Data misfit to (A) post-Landers CMM4 GPS, (B) post-Hector Mine GPS, and (C) all the GPS data. Horizontal and vertical axes show the steady-state viscosity of the upper mantle (η_{UM}) and lower crust (η_{LC}), respectively. The colored lines show the statistical 95% confidence regions of the models with respect to the optimal models marked by the color-coded diamonds with only viscoelastic relaxation (Model 1, red contours), with additional contribution from stress-driven afterslip (Model 2, blue contours), and with additional contribution from kinematic afterslip (Model 3, green contours). The yellow diamond and contour are for Model 2 only constrained by vertical GPS data. The black diamond marks the optimal viscosities without afterslip and without considering the interseismic velocity correction (Liu et al., 2015).

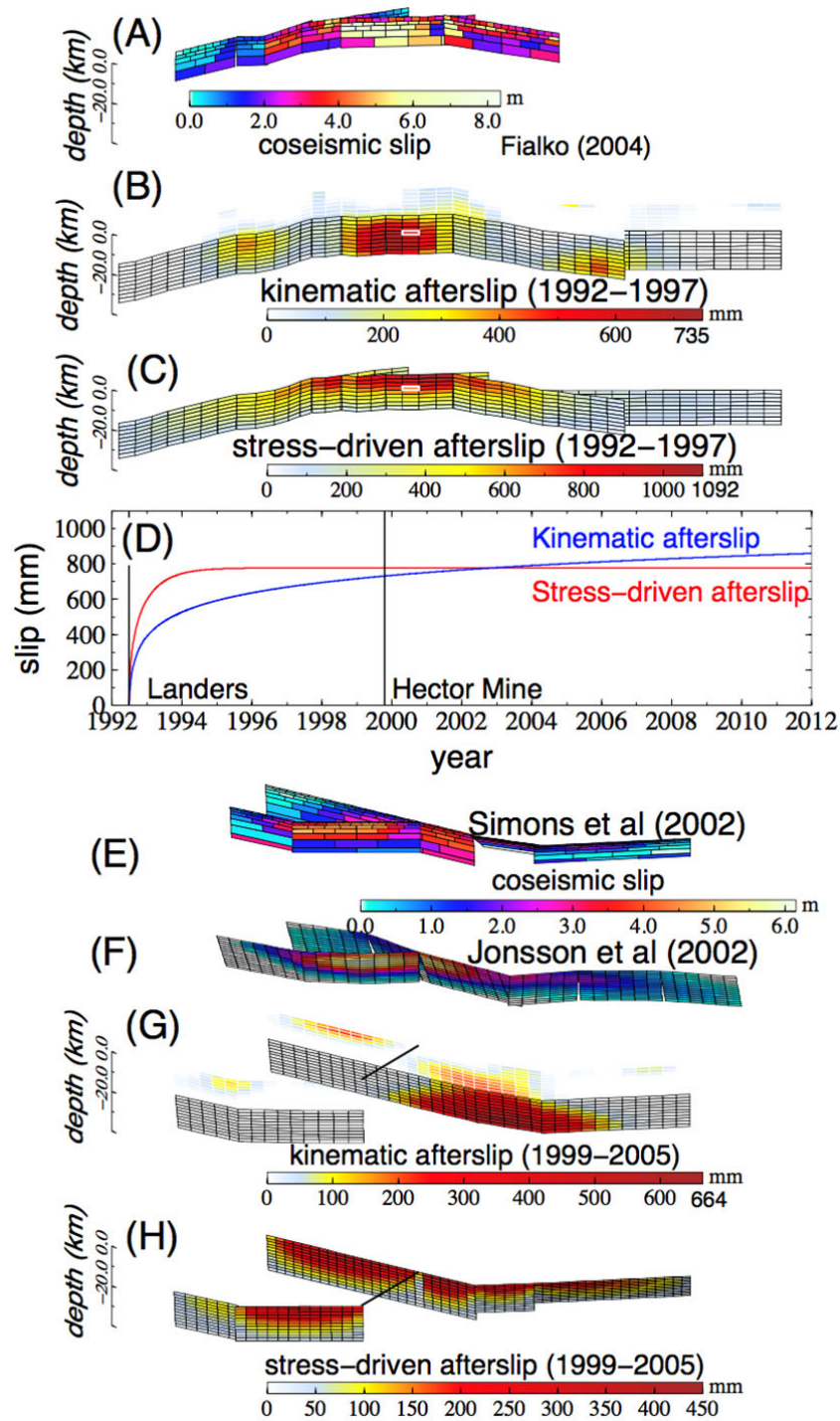


Figure DR11 | Distribution of afterslip for the 1992 Landers and 1999 Hector Mine earthquakes from joint inversion of all the data for afterslip and viscoelastic relaxation (Burgers rheology for the lower crust and upper mantle). 1992 Landers earthquake: (A) Coseismic slip, (B) Kinematic afterslip (1992–1997), (C) Stress-driven deep afterslip (1992–1997), and (D) temporal evolution of afterslip at the selected patch that is marked by white rectangles in (B) and (C). 1999 Hector Mine earthquake: (E–F) Coseismic slip, (G) Kinematic afterslip (1999–2006), and (H) Stress-driven deep afterslip (1999–2005).

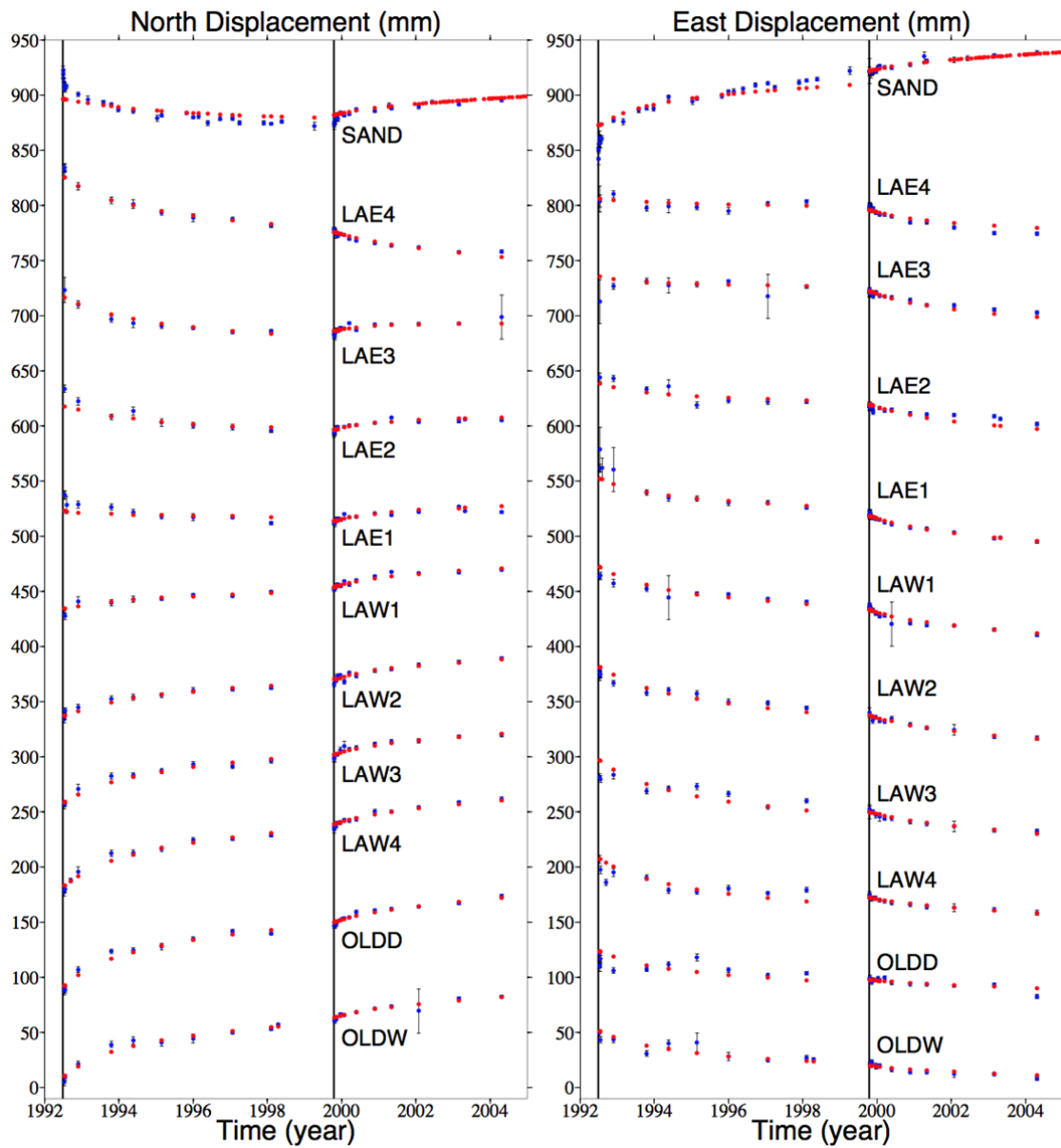


Figure DR12 | Observed (blue dots) and modeled (red dots) displacements for the USGS Emerson Transect in the time period 1992-2004. Model predictions are from viscoelastic relaxation (Burgers rheology).

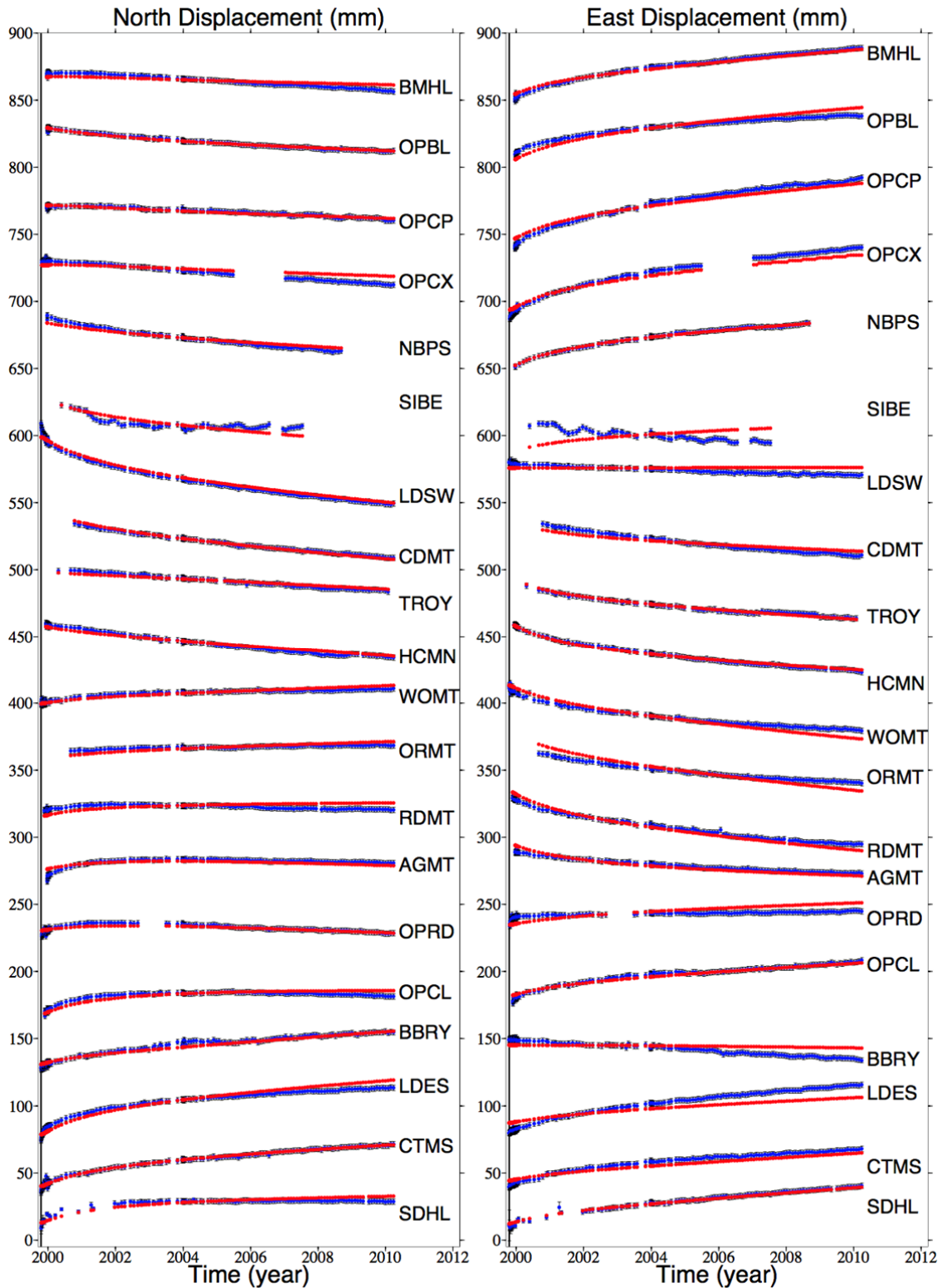


Figure DR13 | Observed (blue dots) and modeled (red dots) displacements for the post-Hector Mine GPS time series. Other details are the same as Figure DR12.

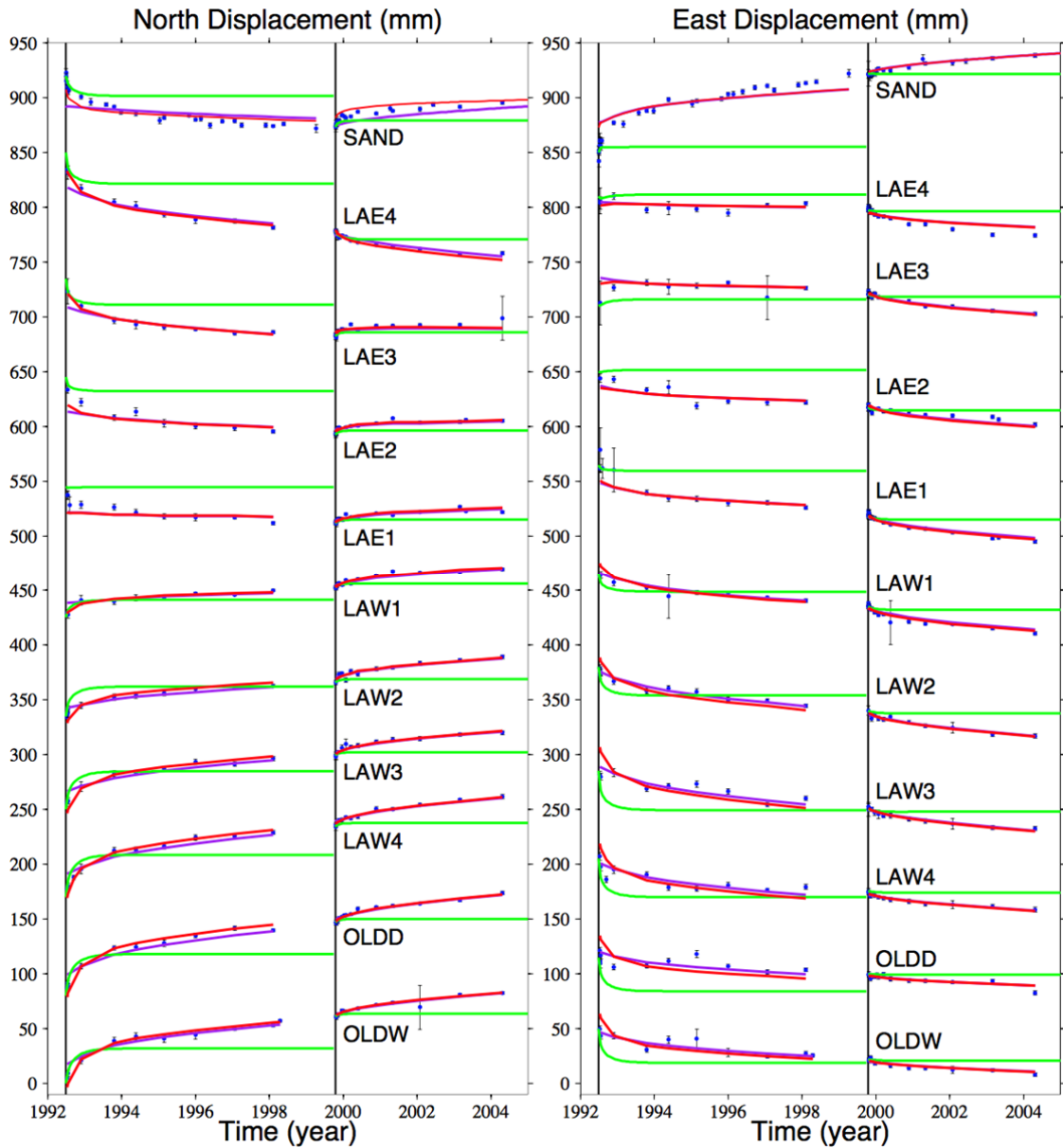


Figure DR14 | Observed time series (blue dots) at the USGS Emerson Transect in the time period 1992-2004, model predictions from stress-driven afterslip (green lines) and viscoelastic relaxation (purple lines for the case with Burgers rheology for the lower crust and upper mantle), and the sum of model predictions from afterslip and viscoelastic relaxation (red lines).

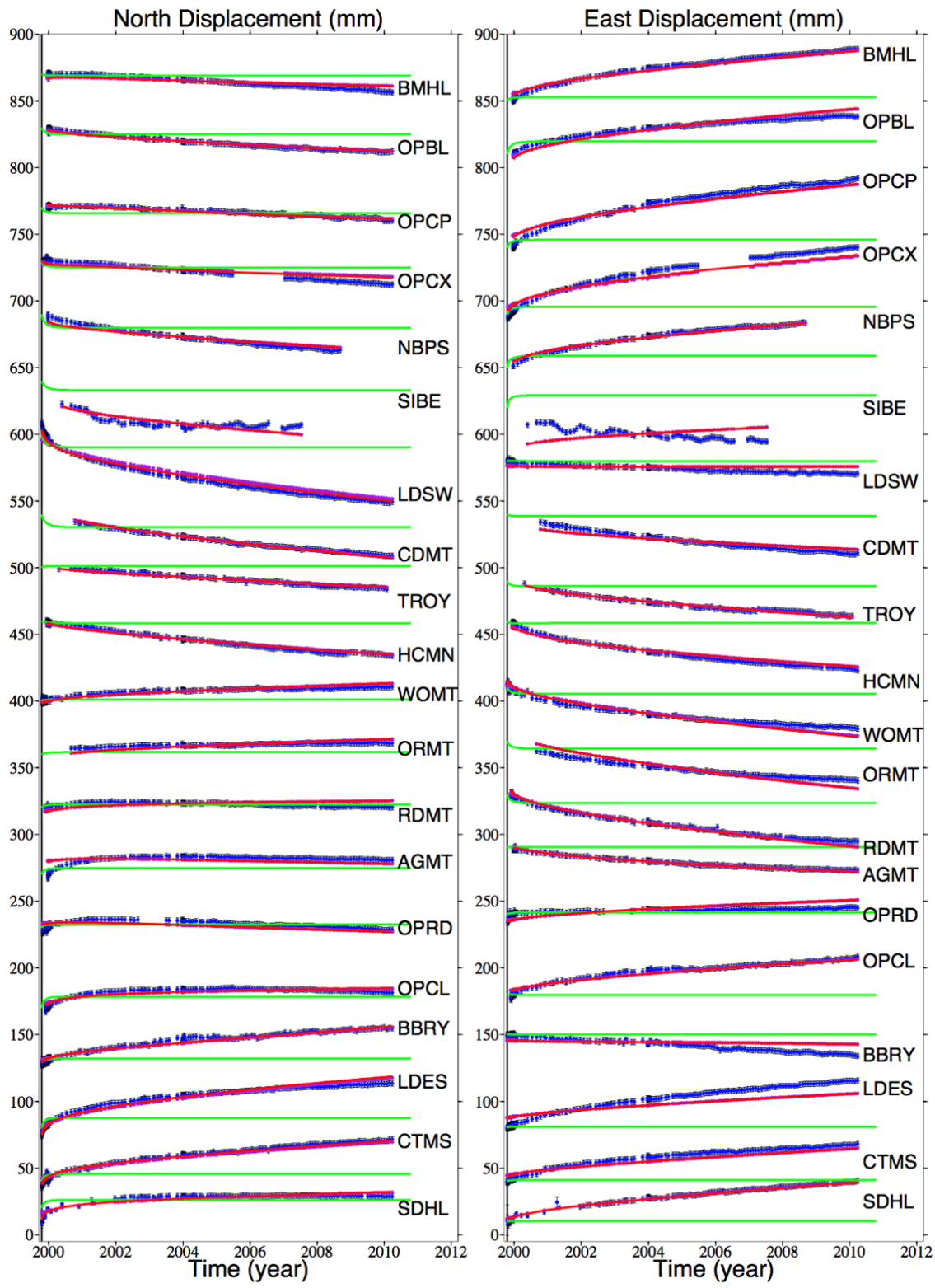


Figure DR15 | Post-Hector Mine GPS time series (blue dots), model predictions from stress-driven afterslip (green lines) and viscoelastic relaxation (purple lines for the case with Burgers rheology for the lower crust and upper mantle), and the sum of model predictions from afterslip and viscoelastic relaxation (red lines).

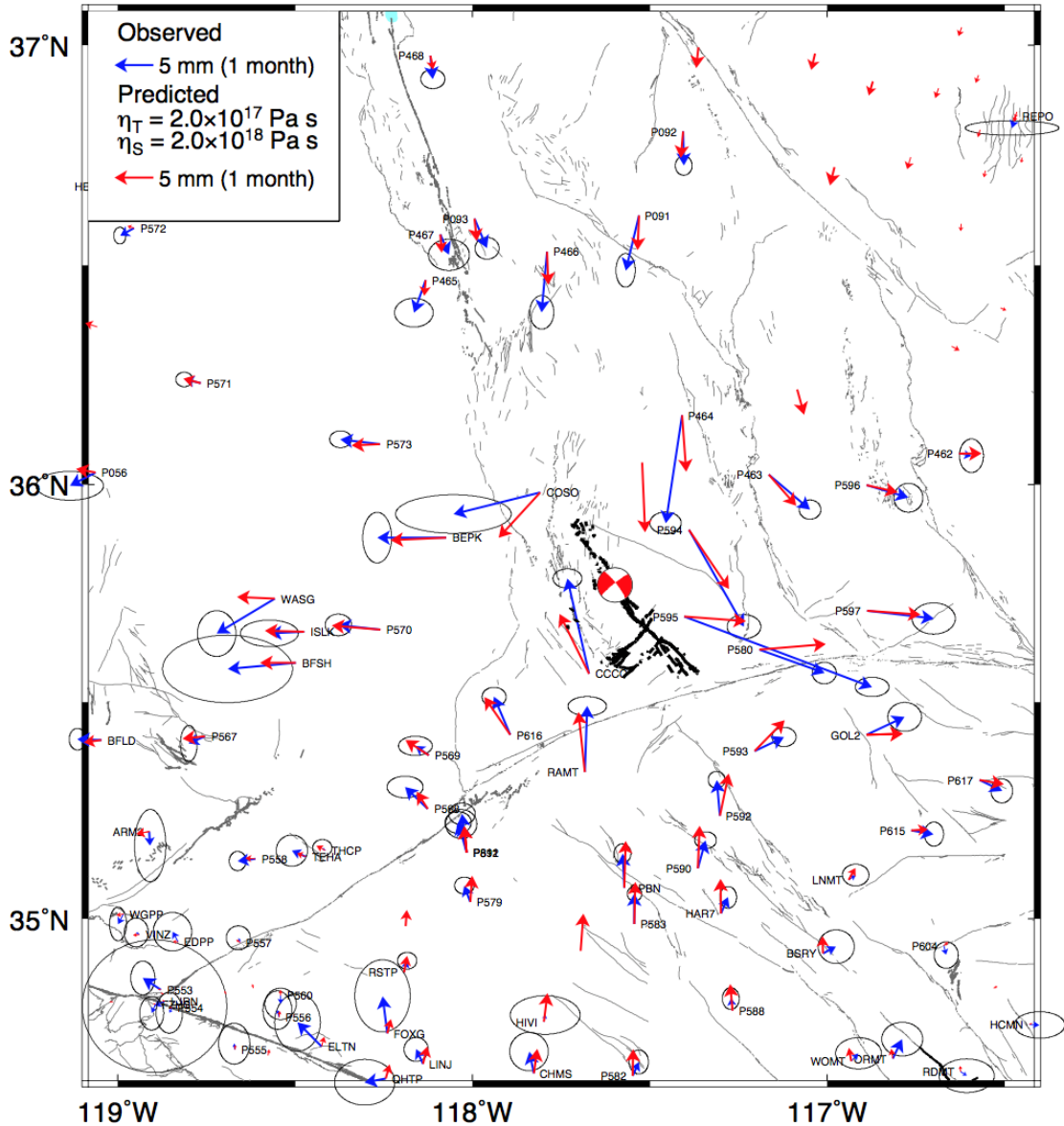


Figure DR16 | Map showing the observed 30 days post-Ridgecrest displacement (blue vectors tipped with 70% confidence ellipses) and model predicted 30 days (red vectors) displacements from only mantle relaxation. The transient and steady-state viscosities of the upper mantle are 2×10^{17} Pa s and 2×10^{18} Pa s, respectively. The observed displacements are not shown for some GPS sites that have no post-Ridgecrest observations. Note the differences in the scales of the vectors. Thick black lines show the surface rupture of the 2019 Ridgecrest sequence.

References

- Barbot, S., Fialko, Y., and Bock, Y., 2009, Postseismic deformation due to the Mw 6.0 2004 Parkfield earthquake: Stress-driven creep on a fault with spatially variable rate-and-state friction parameters: *Journal of Geophysical Research: Solid Earth*, v. 114, no. B7.
- Barbot, S., Moore, J. D. P., and Lambert, V., 2017, Displacement and Stress Associated with Distributed Anelastic Deformation in a Half-Space: *Bulletin of the Seismological Society of America*, v. 107, no. 2, p. 821-855.
- Bürgmann, R., and Dresen, G., 2008, Rheology of the Lower Crust and Upper Mantle: Evidence from Rock Mechanics, Geodesy, and Field Observations: *Annual Review of Earth and Planetary Sciences*, v. 36, no. 1, p. 531-567.
- Deng, J., Gurnis, M., Kanamori, H., and Hauksson, E., 1998, Viscoelastic Flow in the Lower Crust after the 1992 Landers, California, Earthquake: *Science*, v. 282, no. 5394, p. 1689-1692.
- Dickinson-Lovell, H., Huang, M.-H., Freed, A. M., Fielding, E., Bürgmann, R., and Andronicos, C., 2017, Inferred rheological structure and mantle conditions from postseismic deformation following the 2010 Mw 7.2 El Mayor-Cucapah Earthquake: *Geophysical Journal International*, v. 213, no. 3, p. 1720-1730.
- Fialko, Y., 2004a, Evidence of fluid-filled upper crust from observations of postseismic deformation due to the 1992 Mw7.3 Landers earthquake: *Journal of Geophysical Research: Solid Earth*, v. 109, no. B8.
- , 2004b, Probing the mechanical properties of seismically active crust with space geodesy: Study of the coseismic deformation due to the 1992 Mw7.3 Landers (southern California) earthquake: *Journal of Geophysical Research: Solid Earth*, v. 109, no. B3.
- Freed, A. M., Bürgmann, R., and Herring, T., 2007, Far-reaching transient motions after Mojave earthquakes require broad mantle flow beneath a strong crust: *Geophysical Research Letters*, v. 34, no. 19.
- Freed, A. M., Hirth, G., and Behn, M. D., 2012, Using short-term postseismic displacements to infer the ambient deformation conditions of the upper mantle: *Journal of Geophysical Research: Solid Earth*, v. 117, no. B1.
- Herbert, J. W., Cooke, M. L., and Marshall, S. T., 2014, Influence of fault connectivity on slip rates in southern California: Potential impact on discrepancies between geodetic derived and geologic slip rates: *Journal of Geophysical Research: Solid Earth*, v. 119, no. 3, p. 2342-2361.
- Johnson, K. M., Hilley, G. E., and Bürgmann, R., 2007, Influence of lithosphere viscosity structure on estimates of fault slip rate in the Mojave region of the San Andreas fault system: *Journal of Geophysical Research: Solid Earth*, v. 112, no. B7.
- Jones, L. E., and Helmberger, D. V., 1998, Earthquake source parameters and fault kinematics in the eastern California shear zone: *Bulletin of the Seismological Society of America*, v. 88, no. 6, p. 1337-1352.
- Jónsson, S., Segall, P., Pedersen, R., and Björnsson, G., 2003, Post-earthquake ground movements correlated to pore-pressure transients: *Nature*, v. 424, p. 179.
- Jónsson, S. n., Zebker, H., Segall, P., and Amelung, F., 2002, Fault Slip Distribution of the 1999 Mw 7.1 Hector Mine, California, Earthquake, Estimated from Satellite Radar

- and GPS Measurements: *Bulletin of the Seismological Society of America*, v. 92, no. 4, p. 1377-1389.
- Liu, S., Shen, Z.-K., and Bürgmann, R., 2015, Recovery of secular deformation field of Mojave Shear Zone in Southern California from historical terrestrial and GPS measurements: *Journal of Geophysical Research: Solid Earth*, v. 120, no. 5, p. 3965-3990.
- Peltzer, G., Rosen, P., Rogez, F., and Hudnut, K., 1998, Poroelastic rebound along the Landers 1992 earthquake surface rupture: *Journal of Geophysical Research: Solid Earth*, v. 103, no. B12, p. 30131-30145.
- Pollitz, F. F., 2003, Transient rheology of the uppermost mantle beneath the Mojave Desert, California: *Earth and Planetary Science Letters*, v. 215, no. 1, p. 89-104.
- , 2015, Postearthquake relaxation evidence for laterally variable viscoelastic structure and water content in the Southern California mantle: *Journal of Geophysical Research: Solid Earth*, v. 120, no. 4, p. 2672-2696.
- Pollitz, F. F., McCrory, P., Svarc, J., and Murray, J., 2008, Dislocation models of interseismic deformation in the western United States: *Journal of Geophysical Research: Solid Earth*, v. 113, no. B4.
- Pollitz, F. F., Wicks, C., and Thatcher, W., 2001, Mantle Flow Beneath a Continental Strike-Slip Fault: Postseismic Deformation After the 1999 Hector Mine Earthquake: *Science*, v. 293, no. 5536, p. 1814-1818.
- Savage, J. C., and Svarc, J. L., 1997, Postseismic deformation associated with the 1992 M ω =7.3 Landers earthquake, southern California: *Journal of Geophysical Research: Solid Earth*, v. 102, no. B4, p. 7565-7577.
- Shen, Z.-K., Jackson, D. D., Feng, Y., Cline, M., Kim, M., Fang, P., and Bock, Y., 1994, Postseismic deformation following the Landers earthquake, California, 28 June 1992: *Bulletin of the Seismological Society of America*, v. 84, no. 3, p. 780-791.
- Shen, Z.-K., King, R. W., Agnew, D. C., Wang, M., Herring, T. A., Dong, D., and Fang, P., 2011, A unified analysis of crustal motion in Southern California, 1970–2004: The SCEC crustal motion map: *Journal of Geophysical Research: Solid Earth*, v. 116, no. B11.
- Simons, M., Fialko, Y., and Rivera, L., 2002, Coseismic Deformation from the 1999 Mw 7.1 Hector Mine, California, Earthquake as Inferred from InSAR and GPS Observations: *Bulletin of the Seismological Society of America*, v. 92, no. 4, p. 1390-1402.
- Townend, J., and Zoback, M. D., 2000, How faulting keeps the crust strong: *Geology*, v. 28, no. 5, p. 399-402.
- Wald, D. J., and Heaton, T. H., 1994, Spatial and temporal distribution of slip for the 1992 Landers, California, earthquake: *Bulletin of the Seismological Society of America*, v. 84, no. 3, p. 668-691.
- Wang, K., Dreger, D. S., Tinti, E., Bürgmann, R., and Taira, T. a., 2020, Rupture Process of the 2019 Ridgecrest, California Mw 6.4 Foreshock and Mw 7.1 Earthquake Constrained by Seismic and Geodetic Data: *Bulletin of the Seismological Society of America*, v. 110, no. 4, p. 1603-1626.
- Wang, R., and Kumpel, H. J., 2003, Poroelasticity: Efficient modeling of strongly coupled, slow deformation processes in a multilayered half-space: *GEOPHYSICS*, v. 68, no. 2, p. 705-717.
- Wang, R., Lorenzo-Martín, F., and Roth, F., 2006, PSGRN/PSCMP—a new code for calculating co- and post-seismic deformation, geoid and gravity changes based on the

- viscoelastic-gravitational dislocation theory: *Computers & Geosciences*, v. 32, no. 4, p. 527-541.
- Wang, R., Martín, F. L., and Roth, F., 2003, Computation of deformation induced by earthquakes in a multi-layered elastic crust—FORTRAN programs EDGRN/EDCMP: *Computers & Geosciences*, v. 29, no. 2, p. 195-207.
- Xu, X., Tong, X., Sandwell, D. T., Milliner, C. W. D., Dolan, J. F., Hollingsworth, J., Leprince, S., and Ayoub, F., 2016, Refining the shallow slip deficit: *Geophysical Journal International*, v. 204, no. 3, p. 1867-1886.